Department of Physics and Astronomy
University of Heidelberg

Master's thesis
in Physics

submitted by

Paul Birk
born in Odinzovo (Russia)

2016

Time-dependent Strong-Field Effects in Atoms and Molecules observed by Attosecond Transient Absorption Spectroscopy

This master's thesis has been carried out by
Paul Birk
at the
Max-Planck-Institut für Kernphysik
under the supervision of
Prof. Dr. Thomas Pfeifer

Time-dependent Strong-Field Effects in Atoms and Molecules observed by Attosecond Transient Absorption Spectroscopy—In this work, the absorption spectra of an extreme ultraviolet (XUV) attosecond light pulse in argon and molecular nitrogen are investigated as a function of a time delay between the XUV pulse and a near-infrared (NIR) femtosecond light pulse and the NIR peak intensity. The XUV pulses are produced by high-harmonic generation of the NIR pulse yielding attosecond time resolution for the time-delay-dependent absorption spectra. In this all-optical approach, the electronic and vibrational quantum states of the target systems are excited by the weak XUV pulse and dressed by the strong NIR pulse. The strong-field effects, which are observed in the time- and intensity-dependent optical density, are compared between argon and nitrogen. These are line-broadening, line-shape changes, sub-cycle and slower modulations. Emphasis is placed on to the modulations, which originate from two-NIR-photon transitions between different excited states. Furthermore, a focus lies on the intensity-dependent line-shape changes of both species. A measure for these changes is the laser-imposed phase of a wave packet's dipole moment, which is excited by the XUV pulse. This phase is introduced in a dipole-control model and investigated for both species.

Zeitabhängige Effekte starker Felder auf Atome und Moleküle beobachtet mittels Attosekunden zeitaugelöster transienter Absorptionspektroskopie—In dieser Arbeit wird das Absorptionsspektrum eines Attosekunden-Lichtpulses im extrem ultravioletten (XUV) Spektralbereich in Argon und molekularem Stickstoff untersucht. Dies geschieht in Abhängigkeit eines Zeitversatzes zwischen dem XUV-Puls und einem nahinfraroten (NIR) Lichtpuls im Femtosekunden-Bereich und in Abhängigkeit der NIR-Spitzenintensität. Der XUV-Puls wird erzeugt durch Erzeugung hoher Harmonische des NIR-Pulses, was zu einer Zeitauflösung im Attosekunden-Bereich für das zeitabhängige Absorptionspektrum führt. Bei diesem rein optischen Ansatz werden die elektronischen und vibronischen quantenmechanischen Zustände des Target-Systems mit Hilfe des XUV-Pulses angeregt und mit dem starken NIR-Puls manipuliert. Die Effekte der starken Felder auf Argon und Stickstoff, welche in der zeit- und intensitätsabhängigen optischen Dichte beobachtet werden, werden verglichen. Dabei handelt es sich um Linienverbreiterungen, Änderungen der Linienform, unterzyklische und langsame Modulationen. Ein besonderer Schwerpunkt wird auf die Modulationen gelegt, welche von Übergängen zwischen verschiedenen angeregten Zuständen mit zwei NIR-Photonen stammen. Weiterhin liegt ein Fo-

kus auf der intensitätsabhängigen Änderung der Linienform beider Stoffe. Ein Maß für diese Änderungen stellt die Phase dar, welche dem Dipolmoment eines durch den XUV-Puls angeregten Wellenpakets aufgprägt wird. Nach der theoretischen Einfügung dieser Phase in einem sogenannten Dipol-Kontroll-Model, wird diese für beide Stoffe untersucht.

Contents

1 Introduction

How do intra-atomic and molecular processes evolve in time? In order to answer this question, one has to understand the physics and time scales, which govern the evolution of such microscopic systems. Whereas motion in the macroscopic world, which we know from daily life, can essentially be described by means of classical mechanics, the evolution of microscopic system has to be treated quantum-mechanically. Here, motion is described by the phase evolution of the system's quantum states and the time scales, during which these take place, are determined by the energy differences of these states.

Quantum mechanics provides a natural constant as a conversion factor between these energy differences and time scales, which is the Planck constant $h \approx 4.14 \cdot 10^{-15}$ eV*s. Thus, considering for example the vibrational motion of the nuclei in a molecule, whose quantum states typically have energy differences in the order of a few to hundreds of millielectronvolts, the time scales are in the order of femtoseconds (1 fs = 10^{-15} s). The evolution of electronic states is much faster. Here, the energies can lie in the range of tens of electronvolts, which corresponds to the attosecond (1 as = 10^{-18} s) time scale.

In order to study dynamical processes of atomic or molecular systems, one needs therefore a controllable tool, that lives on the same time scale. A successful approach is to use ultrashort light pulses and to study their interaction with matter with a high temporal resolution. Gaining knowledge about this light-matter interaction gives access to understand, manipulate or even control microscopic systems in a systematic way. With the advent of extreme ultraviolet light pulses in the attosecond time regime produced by high-order harmonic generation of near-infrared light, one nowadays has access to electronic state dynamics [1]. A broad bandwidth in the spectral range is needed for the production of short light pulses, which brings the advantage that the system can be excited with a broad range of energies at a certain instant in time, producing a superposition of quantum states and thereby inducing wave-packet dynamics.

A common method is to use ultrashort light pulses in a pump-probe scheme [2]. Here, a target system is excited to a certain quantum state or a superposition of states by the first pump pulse and after some evolution time the second pulse probes the system. An observable is then investigated as a function of the time delay between the two pulses, which yields information about the dynamics of the system during this evolution time. The typical experiments focus on the femtosecond time scale and, for example, vibrational dynamics in molecules have been extensively studied [2]. In order to measure electron dynamics, an alternative approach became successful, which is the attosecond transient absorption spectroscopy (ATAS). In ATAS the transmission of a broadband attosecond pulse through a target system is measured spectroscopically with respect to the time delay of a second femtosecond pulse, which perturbs the target. By means of this all optical approach it has been possible to gain a lot of fundamental knowledge about light-matter interactions, bound-state dynamics or electron correlations in atoms. For example, the motion of valence electrons in krypton could be observed in real time [3] or it was possible to reconstruct and control two-electron wave-packets [4]. A prototype target in ATAS is helium, in which, among others, sub-cycle ac Stark shifts [5] or light-induced states [6] could be observed. The experiments with ATAS are still on a basic research level. However, by and by some promising applications or at least promising attempts arise, for example ultrafast electronic switches [7].

Extending the knowledge about ATAS from atomic systems to molecular systems provides interesting prospects: The properties of chemical bonds in molecules are governed by the states and the phases of their electrons. A well-known and illustrative example for this is the hydrogen molecular ion. There are two possibilities for the ground-state electronic wave function, which are the bonding and the antibonding functions. These functions differ just by a relative phase. By getting access to the evolution of these electron's phases, e.g. with the help of attosecond pulses, one could gain insight into the properties, the formation or the break up of molecules. This leads to the idea of attochemistry [8] [9]. An interesting proposal, for example, is the time-resolved study of electrons propagating through conical intersections of potential energy surfaces in molecules [10]. At these intersections the well-known Born-Oppenheimer approximation breaks down and therefore many molecule formation processes are mediated by these intersections. Hence, attosecond-resolved studies in

molecules would be far-reaching and ATAS is a promising tool to enter this field of research. However, the development of theories and successful experiments of ATAS in molecules is just starting [11–15].

This thesis presents the first ATAS experiment in molecules in the extreme ultraviolet spectral range, which is able to tune the NIR intensity from a perturbative to a strong-field regime. Since many effects in ATAS in atomic systems are already known, this work uses a bottom-up approach and compares time and near-infrared-intensity dependent strong-field effects in atomic argon and molecular nitrogen. Both species have their first ionization threshold in a similar energy range at about 15.5 eV, which makes them readily comparable in a single experiment. Almost all experiments in ATAS cover energies above 20 eV due to the availability of convenient filters and gratings. By an upgrade of the experimental setup presented in this thesis, the energy range down to 13 eV has become accessible, which covers the interesting single-excitation region of argon and nitrogen.

In this thesis, first the theoretical basics of ultrashort light pulses and their interaction with matter are briefly introduced. Afterwards, the setup, which was used for the ATAS experiment performed within this work, is presented. Here, the new grating holder and the properties of the newly installed indium filters, which were needed for the accessibility of the absorption spectrum below 20 eV, are shown. In the third chapter, the procedures of the data acquisition and calibration are explained, where methods for the energy-axis calibration and for a better displaying of the Fourier spectra were developed. At the end, the measurement results and the first evaluation of the time- and intensity-dependent absorption spectra in argon and nitrogen are presented. Emphasis is given to the oscillatory modulation of the optical density and the line-shape changes with respect to the peak intensity of the near-infrared laser pulse.

2 Fundamentals

For the study of ultrashort processes in nature, their dynamics have to be probed with a timing reference on the same time scale. In state-of-the-art experiments this timing reference is provided by an ultrashort laser pulse, which interacts with the medium under investigation. This section introduces the basic mathematical description to treat these laser pulses and their interactions with matter in the context of this work. More detailed descriptions covering the research area of ultrafast phenomena can be found in many textbooks like [16–18] or review articles like [19–21]. Section 2.1 deals with the basics of laser pulses and after introducing the ponderomotive potential, section 2.3 describes the production of attosecond light pulses, which are the shortest light pulses one can produce so far [22]. Nevertheless, they can mathematically be treated like conventional laser pulses and can therefore also be described within the presented framework. A fruitful measure for light-matter interaction is the photoabsorption cross-section, which is the subject of the last three sections. The changes introduced to the shape of the cross-sections at resonance energies by an interaction between an intense near infrared laser pulse and the target are of particular interest. In order to quantify these changes, the dipole control model is introduced at the end of this section.

2.1 Ultrashort light pulses

The time-dependent electric field at a specific point in space $E(t)$ of a linearly polarized laser pulse can be written as the product of an envelope $\mathcal{E}(t)$ and a phase term:

$$E(t) = \mathcal{E}(t) \cdot e^{i\phi(t)} \tag{2.1}$$

It is more convenient to use the complex representation of the electric field. The corresponding physical value is then the real part of the complex function.

In general the envelope can have an arbitrary shape. However, in many analytical descriptions and also for estimation purposes in the experiment, it is approximated by a Gaussian function:

$$\mathcal{E}_{\text{Gauss}}(t) = \mathcal{E}_0 e^{-2\ln(2)\cdot(\frac{t}{\tau})^2}, \tag{2.2}$$

where $\mathcal{E}_0$ is the peak amplitude and τ is the full width at half maximum (FWHM) of the pulse. The intensity profile of such a pulse then reads:

$$I(t) = I_{\text{peak}} e^{-4\ln(2)\cdot(\frac{t}{\tau})^2}, \tag{2.3}$$

with the peak intensity

$$I_{\text{peak}} = \frac{1}{2}\epsilon_0 c \mathcal{E}_0. \tag{2.4}$$

Here, ϵ_0 is the electric vacuum permittivity and c is the speed of light. The peak intensity can be related to the pulse energy ϵ, the time duration τ and the beam waist diameter w. In case of Gaussian beam profiles the relation is:

$$I_{\text{peak}} = \frac{1.88}{\pi}\frac{\epsilon}{\tau w^2}. \tag{2.5}$$

Thus, in order to obtain high peak intensities, one can either increase the pulse energy, compress the pulse in time or focus the pulse to a smaller spot size.

The phase ϕ in equation 2.1 can usually be expanded in terms of a power series:

$$\phi(t) = \phi_{\text{CEP}} + \omega_c t + bt^2 + \dots \tag{2.6}$$

The constant phase term ϕ_{CEP} is the offset between the maximum of the carrier wave and the pulse envelope and is therefore called the carrier-envelope phase (CEP). In few-cycle laser pulses the CEP greatly influences the shape and the maximum intensity of the pulse itself. ω_c is the central frequency of the carrier wave and b is the chirp parameter. By defining the instantaneous frequency of the wave

$$\omega(t) = \frac{\mathrm{d}\phi(t)}{\mathrm{d}t} = \omega_c + 2bt + \dots, \tag{2.7}$$

the function of b is revealed. For $b > 0$, the frequency increases in time, the pulse is called up-chirped and for $b < 0$ it decreases and the pulse is accordingly called down-chirped. Higher terms in equation 2.6 describe chirps of higher order like third or even fourth order chirp. If all these chirp parameters are zero, the pulse will be called transform limited, which means it possesses the shortest time duration supported by the spectral bandwidth. The relationship between wavelength bandwidth and pulse duration then reads for a Gaussian pulse:

$$\Delta\lambda = \frac{2\ln 2}{\pi c}\frac{\lambda_c}{\tau}, \tag{2.8}$$

with the central wavelength λ_c. Using these short pulses for time resolved spectroscopy provides high time-resolution as well as a broad range of frequencies one can investigate with using a single laser system. Thus, by shining these pulses on a target, e.g. a molecular gas, many quantum states $|\psi_n\rangle$ of the system are excited simultaneously producing an electronic, vibronic or rotational wave packet:

$$|\Psi\rangle = \sum_n c_n|\psi_n\rangle. \tag{2.9}$$

This wave packet usually leads to a non-vanishing dipole moment, which is defined as:

$$\mu = \langle\Psi|e\hat{r}|\Psi\rangle, \tag{2.10}$$

where e is the elementary charge and $\hat{r}$ is the position operator of the electrons with respect to the center of charge of the nuclei. Since the individual phases of the quantum states evolve with their resonance energy E_{res} and the states decay to the ground state with the decay rate Γ, the dipole moment is in general time dependent. By considering only a single excited state and the ground state the dipole moment is:

$$\mu = \mu(t) \propto i\exp\left(-\frac{\Gamma}{2}t + i\frac{E_{\text{res}}}{\hbar}t\right). \tag{2.11}$$

The physical value of the dipole moment is, like in the electric field case, the real part of this complex function.

2.2 Ponderomotive potential

The ponderomotive potential is a quasi potential that a free electron experiences if it is exposed to an oscillating electric field $E(t)$. If the electron is bound in an atomic or molecular system, the concept of the ponderomotive potential will be approximately applicable if the electron is in a highly excited state and can therefore be considered as quasi free. The electric field leads to an acceleration of the electron's motion:

$$\ddot{x}(t) = -\frac{eE(t)}{m_e}, \tag{2.12}$$

where m_e is the electron mass. If the electric field can be expressed by a plain wave, i.e. $E(t) = E_0 \cos(\omega_c t + \phi)$, solutions for the velocity and the position will be obtainable by an analytical integration. With the initial condition $x(0) = 0$ and $\dot{x}(0) = 0$ one gets:

$$\dot{x}(t) = -\frac{e\mathcal{E}_0}{m_e\omega_c}[\sin(\omega_c t + \phi) - \sin(\phi)], \tag{2.13}$$

$$x(t) = -\frac{e\mathcal{E}_0}{m_e\omega_c^2}[-\cos(\omega_c t + \phi) + \cos(\phi)] + \frac{e\mathcal{E}_0}{m_e\omega_c} t \sin(\phi). \tag{2.14}$$

Both equations consist of a quivering motion by the first term and a drift motion, the second term, where the quiver amplitude is given by

$$x_0 = -\frac{e\mathcal{E}_0}{m_e\omega_c^2}. \tag{2.15}$$

The drift motion parts are influenced by the electric field phase ϕ at time $t = 0$ and determine whether and how often an electron comes back to its parent ion if it is ionized by the electric field. The ponderomotive potential U_P is defined as the cycle averaged kinetic energy of the electron:

$$\begin{aligned} U_\mathrm{P} = \left\langle E_{kin} \right\rangle &= \frac{m_e}{2}\left\langle \left[-\frac{e\mathcal{E}_0}{m_e\omega_c}[\sin(\omega_c t + \phi) - \sin(\phi)]\right]^2 \right\rangle \\ &= \frac{e^2\mathcal{E}_0^2}{4m_e\omega_c^2} = \frac{e^2}{2c\epsilon_0 m_e}\lambda_c^2 I. \end{aligned} \tag{2.16}$$

U_P is proportional to the intensity and to the wavelength squared of the electric field and can thus be controlled in an experiment. Furthermore, U_P lifts up the ionization potential, so that one has to overcome the effective potential:

$$\tilde{I}_\mathrm{P} = I_\mathrm{P} + U_\mathrm{P} \tag{2.17}$$

in order to liberate an electron out of an atomic or molecular target by an intense laser pulse.

2.3 Generation of attosecond pulses in the extreme ultraviolet spectral range

In order to temporally resolve the dynamics of electronic wave-packets, one needs light pulses with durations of the electronic natural attosecond time scale. Furthermore, to get access to the resonance energy of the systems, which are usually in the order of several electron volts one needs pulses with a frequency bandwidth that covers the vacuum ultraviolet or extreme ultraviolet (XUV) spectral range. The process of high harmonic generation (HHG) became a working horse for the production of such pulses in a table top setting [20, 21]. Despite the high-order nonlinear process of HHG its principles can be described by a quasi-classical three step model introduced by P. Corkum in 1993 [23]. This model is illustrated in figure 2.1. Here, a conversion medium, most often a rare gas, is exposed to the oscillating electric field of a strong femtosecond laser pulse. If the laser pulse is intense enough, i.e. the intensity is in the order of $10^{14}\,\mathrm{W/cm^2}$, the electric field will be able to deform the atomic coulomb potential such that parts of the electronic wave function can tunnel trough the coulomb barrier into the continuum. These free parts are forced away from their parent ion by the electric field and thereby gain kinetic energy. After a half cycle, the electric field switches its sign and the free parts of the wave function are driven back to the ionic core, where they can interfere with the remaining bound parts. This interference leads to a fast oscillating electron density and therewith an oscillating dipole moment, which emits high-energetic photons with the energy:

$$\hbar\omega_\mathrm{HHG} = E_\mathrm{kin} + I_\mathrm{P}, \tag{2.18}$$

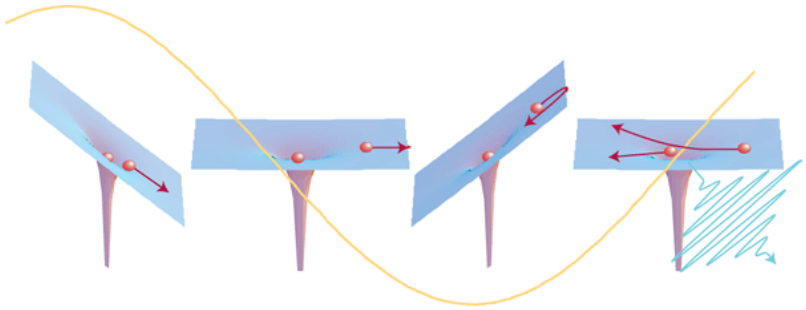

Figure 2.1: Sketch of the three step model. The cycle of the electric field is indicated by the yellow curve and the electronic wave functions by red particles. The electric field deforms the Coulomb potential of the target, so that parts of the electronic wave function can leave the potential, gain kinetic energy as a free particle and drop back to the parent ion resulting in an emission of a high energetic photon (the blue field). The figure is adapted from reference [25].

where I_P is the ionization energy of the conversion gas. The amount of the kinetic energy depends on the trajectory of the free wave function. A classical calculation yields the limit:

$$E_{\mathrm{kin,max}} = 3.17\, U_p. \tag{2.19}$$

This limit determines the energy cutoff of the harmonics and since U_p is proportional to the laser intensity and the wavelength squared of the fundamental laser pulse, equation 2.16, high driving-laser intensities and long wavelengths are needed for high photon energies. Because the efficiency drops for very high wavelengths, driving laser pulses in the near infrared or visible spectral region have been established for experiments which use HHG [24].

2.4 Linear absorption

When an electromagnetic wave with electric field $E(t, z)$ propagates trough a material with polarization P the scalar wave equation for the field becomes

$$\left[\frac{\partial^2}{\partial z^2} - \frac{1}{c^2}\frac{\partial^2}{\partial t^2}\right] E(t,z) = \mu_0 \frac{\partial^2}{\partial t^2} P(t,z), \tag{2.20}$$

where μ_0 is the vacuum permeability. In atomic or molecular gases as interaction medium the polarization can be traced back to the averaged dipole moment μ per atom/molecule

$$P = \langle \mu \rangle \cdot \rho_N, \tag{2.21}$$

with the number density $\rho_N = N/V$. A non-vanishing dipole moment is induced in the target if a superposition of electronic states is excited by the electromagnetic wave. In equation 2.20 the polarization acts like a source of the electric field, which interferes with the medium-free field leading to a modification of the electromagnetic wave. The spectrum of this modified wave is the measured quantity in many time-resolved absorption experiments. The linear polarization can be related to the electric field in the frequency domain by

$$\tilde{P}(\omega) = \epsilon_0 \chi(\omega) \cdot \tilde{E}(\omega), \tag{2.22}$$

where $\chi(\omega)$ is the frequency dependent linear electric susceptibility of the medium. It is conventionally described as a complex quantity:

$$\chi(\omega) = \chi'(\omega) + i\chi''(\omega). \tag{2.23}$$

In the frequency domain the solution of 2.20 then becomes

$$\tilde{E}(\omega, z) = \tilde{E}(\omega, 0) e^{-ik(\omega)z}, \tag{2.24}$$

where the frequency dependent wave vector $k(\omega)$ can be expressed by

$$k(\omega) = \frac{\omega}{c}\tilde{n}(\omega) = \frac{\omega}{c}\sqrt{1 + \chi'(\omega) + i\chi''(\omega)}, \tag{2.25}$$

with $\tilde{n}(\omega)$ as the complex refractive index. Since the spectroscopic targets in this work are dilute gases, the material can usually be treated as weakly absorbing, i.e. $\chi', \chi'' \ll 1$. Thus, the imaginary part of equation 2.25, which describes the absorption of the material can be approximated by

$$\alpha(\omega) = 2 \cdot \mathrm{Im}\left[\frac{\omega}{c}\sqrt{1 + \chi'(\omega) + i\chi''(\omega)}\right] \approx \frac{\omega}{c}\chi''. \tag{2.26}$$

The frequency dependent absorption coefficient $\alpha(\omega)$ enters into the well known Lambert-Beer's law

$$I(\omega, z) = I_0(\omega)e^{-\alpha(\omega)z}. \tag{2.27}$$

Therefore, by measuring the incident light intensity $I_0(\omega)$ and the attenuated intensity $I(\omega, z)$ after interaction length z one gets direct access to the macroscopic and microscopic electric field response of the target material. In defining the absorption cross-section $\sigma(\omega)$ by the absorption coefficient per number density ρ_N of the target gas, the macroscopic cross-section is in summary related to the microscopic dipole moment by

$$\sigma(\omega) = \frac{\alpha}{\rho} = \frac{\omega}{\epsilon_0 c}\mathrm{Im}\left(\frac{\langle\tilde{\mu}(\omega)\rangle}{\tilde{E}(\omega)}\right) \tag{2.28}$$

The data measured in the experiment is commonly represented in optical density (OD), which is related to the cross-section by

$$\mathrm{OD}(\omega) = \log_{10}\left(\frac{I_0(\omega)}{I(\omega)}\right) = \frac{\sigma(\omega)}{\ln 10} \cdot \rho_N \cdot l \tag{2.29}$$

where l is the thickness of the sample.

2.5 Fano profiles

In absorption spectroscopy, the natural symmetric Lorentzian line shapes are commonly observed in many atomic or molecular targets. However, at sufficient resolution some lines appear in an asymmetric fashion. They are called Fano profiles, named after Ugo Fano, who was the first to theoretically explained the origin of this asymmetry in a very general manner [26]. In a nutshell, it is based on the interference of at least two quantum pathways with the same initial and finale state. A simple and instructive example is an autoionizing state of a system with two electrons like helium. This system has quasi-stationary states, where both electrons are excited. These doubly excited states are degenerate in energy with a continuum state, where one electron is in the original 1s ground state and the other is in the continuum. This degeneracy leads to a configuration interaction of both states and consequently to the autoionization of the doubly excited states by ejection of one electron and the de-excitation to

the ground state of the other. Thus, there are two possible quantum pathways for ionizing the helium atom at the resonance energy. One way is the direct photoionization and the other is the intermediate excitation to the doubly excited states with the subsequent autoionization. On these pathways, the system acquires different phases, which lead to a not completely destructive or constructive interference and hence to an asymmetric line shape seen in the photoabsorption cross-section. The relation between the transition amplitudes of both pathways defines the so called Fano q-parameter:

$$q = \frac{\langle e|\hat{T}|g\rangle}{\pi V^* \langle c|\hat{T}|g\rangle}, \tag{2.30}$$

where $|g\rangle$, $|e\rangle$ and $|c\rangle$ are the ground, excited and continuum state, respectively and $\hat{T}$ is the transition operator. The relation is scaled by the configuration interaction $V = \langle c|\hat{H}|e\rangle$ with the systems Hamilton operator $\hat{H}$. The q-parameter directly determines the shape of the photoabsorption cross-section of the resonance:

$$\sigma \propto \frac{(q+\epsilon)^2}{1+\epsilon^2}. \tag{2.31}$$

Here ϵ is the reduced energy:

$$\epsilon = \frac{E - E_{res}}{\hbar\Gamma/2}, \tag{2.32}$$

where $\hbar\Gamma$ denotes the line width of the resonance. Figure 2.2 illustrates the photoabsorption cross-section for different q-parameters. The lines are left–right symmetric with respect to the sign of q. For $q = 0$ the lineshape becomes the inverted Lorentzian, while for $q \to \pm\infty$ the lines converge against the common Lorentz line.

2.6 The dipole control model

In section 2.4, it was shown that the photoabsorption cross-section gives direct access to the imaginary part of the microscopic dipole response of the spectroscopic target $\sigma(\omega) \propto \mathrm{Im}[\langle\tilde{\mu}(\omega)\rangle]$. Thus, the asymmetry of the absorption lines discussed in the previous section has to have an explicit signature in

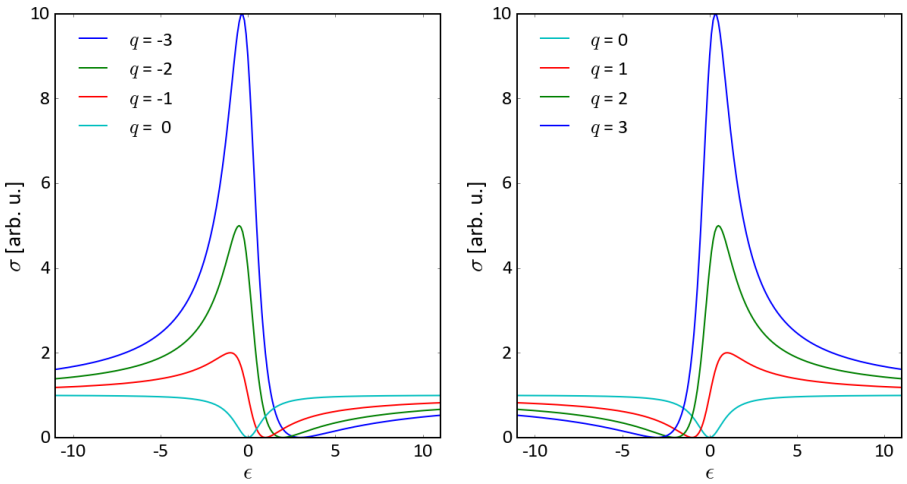

Figure 2.2: The photoabsorption cross-section for different Fano q-parameters versus the reduced energy acording to eguation 2.31.

the time dependent dipole moment. It was shown that the Fano q-parameter corresponds directly to an initial phase ϕ_{Fano} of the dipole moment [27]:

$$\mu(t) \propto i \exp\left(-\frac{\Gamma}{2}t + i\frac{E_{\text{res}}}{\hbar}t + i\phi_{\text{Fano}}(q)\right), \tag{2.33}$$

with the direct relations:

$$\phi_{\text{Fano}}(q) = 2 \cdot \arg(q - i) \qquad \text{or} \qquad q(\phi_{\text{Fano}}) = -\cot\left(\frac{\phi_{\text{Fano}}}{2}\right). \tag{2.34}$$

Since the phase is preserved in the Fourier transformation of the dipole moment:

$$\tilde{\mu}(\omega) = \int_{\infty}^{\infty} \mu(t) e^{-i\omega t} \mathrm{d}t \propto \frac{i}{i(\hbar\omega - E_{\text{res}}) + \hbar\Gamma/2} \cdot e^{i\phi_{\text{Fano}}(q)}, \tag{2.35}$$

a zero phase shift will result in the well know Lorentzian function of the energy dependent dipole moment. By controlling this initial phase, it was possible to tune q and thereby the absorption line shape at will from Fano to Lorentz and vice versa. This was done by means of a strong NIR pulse, which dresses the spectroscopic target after excitation by a broadband XUV pulse and thus disturbs the freely decaying dipole [27]. The system's states acquire additional

phases by means of their respective energy shifts ΔE, which arise from the ac-Stark shift or for high Rydberg states approximately by the ponderomotive potential [28]:

$$\phi_{\text{Laser}} = \Delta\phi_{\text{Fano}} = \int_0^T \frac{\Delta E}{\hbar}\mathrm{d}t, \tag{2.36}$$

where T is the time it takes for the energy shift to occur e.g. the pulse duration of the NIR. In the treatment here, the phase shift is impulsive at the instant of excitation of the dipole moment. In a recent work by Blättermann et.al. [29] it was accounted for the time delay between the dipole excitation and the moment of phase shifting, which reflects the pulse sequences in an attosecond transient absorption spectroscopy experiment in a more appropriate way, because in such experiments the time delay of the NIR pulse is scanned with respect to the exciting XUV pulse. In the new model, called dipole control model, the time dependent dipole response is split into two parts. The first describes the freely decaying dipole starting at time $t = 0$ and it is replaced by a phase shifted free decaying dipole at time $t = \tau$ when the dressing laser pulse arrives:

$$\mu(t,\tau) \propto \begin{cases} i\exp\left(-\frac{\Gamma}{2}t + i\frac{E_{\text{res}}}{\hbar}t\right) & \text{for } 0 < t < \tau \\ i\exp\left(-\frac{\Gamma}{2}t + i\frac{E_{\text{res}}}{\hbar}t\right)\cdot\exp(i\phi_{\text{Laser}}) & \text{for } \tau < t \end{cases} \tag{2.37}$$

In addition, an amplitude in front of the phase, which is for simplicity not included here, can account for ionization and resonant couplings in the time delay spectra [30]. For times $t < 0$ the dipole vanishes, because no wavepacket has been excited yet. By means of Fourier transformation, the according spectroscopic signal, which results from this method, can be retrieved. The transformation can even be done analytically:

$$\sigma(\omega,\tau) \propto \text{Im}\left[\tilde{\mu}(\omega,\tau)\right] = \text{Im}\left[\int_\infty^\infty \mu(t,\tau)e^{-i\omega t}\mathrm{d}t\right] \tag{2.38}$$

$$\propto \text{Im}\left[i\frac{1 - e^{i\frac{E_{\text{res}}-E}{\hbar}\tau - \frac{\Gamma}{2}\tau}(1 - e^{\phi_{\text{Laser}}})}{i(E - E_{\text{res}}) + \hbar\Gamma/2}\right]. \tag{2.39}$$

With the abbreviations for the detuning $\delta = (E - E_{\text{res}})/\hbar$ and the linewidth $\gamma = \Gamma/2$ the equation can be cast in the final compact form with a similar notation as compared to the work in [30]:

$$\sigma(\omega,\tau) \propto \text{Im}\left[-\frac{1 - e^{-i\delta\tau - \gamma\tau}(1 - e^{\phi_{\text{Laser}}})}{\delta - i\gamma}\right]. \tag{2.40}$$

By fitting this equation to the time-delay or intensity dependent spectra, the laser-imposed phase ϕ_{Laser} can be retrieved, which gives a measure for the microscopic light-matter interaction. In the dipole control model only one nucleus is considered. Thus, when dealing with molecules, the existence of at least two nuclei might lead to deviations from this model. However, in case of high valence or Rydberg states, the electron should see effectively a single nucleus and this approach can still be applied.

3 Experimental Setup

The production of attosecond light pulses in the extreme ultraviolet (XUV) spectral range by high harmonic generation (HHG) requires the interaction between a laser pulse preferentially in the near infrared (NIR) spectral region with high peak intensity and an atomic or molecular ensemble as conversion medium. High peak intensities in the order of 10^{14} W/cm^2 can be reached by combining high pulse energies with ultra-short pulse durations and small focal spot sizes. Thus, one needs several pulse amplification and pulse-duration compression steps in a single laser system. In this experiment in addition the fundamental of the HHG is used to dress, manipulate or control a target ensemble which is spectroscopically investigated by the XUV pulse. This chapter describes the technical aspects of the experimental setup in this work including the production and manipulation of the fundamental few cycle NIR pulse for time-delay and intensity-dependent transient absorption spectroscopy. Parts of the experimental setup are also discussed in previous work in more detail, see e.g. [31, 32].

3.1 NIR laser system

The experimental setup starts with the commercially available laser system Femtopower compact Pro CEP by FEMTOLASERS Produktions GmbH. The CEP stabilization was not used and is actually not needed in the experiment performed in this work. The 'Rainbow' oscillator consists of a titanium doped sapphire crystal in a mode-locking cavity geometry and is pumped by a Verdi V6 by Coherent, Inc. (figure 3.1 a)). It provides a laser pulse (seed pulse) of sub-10 fs duration with a continuous octave-spanning spectrum at 800 nm central wavelength and a pulse energy of a few nJ at a repetition rate of about 80 MHz.

In order to amplify the input pulse to the pulse energy required for HHG

a second titanium-sapphire crystal is used in 9-pass configuration pumped by a high power Q-switched laser (DM-30 by Photonics Industries International, Inc.), see figure 3.1 b). A pockels cell triggered by the DM-30 picks up a single pulse of the seed after the 4th path to get a synchronized seed-amplifier system at 4 kHz repetition but increased 0.8 mJ pulse energy. In order to prevent the amplifier crystal from damage due to the high peak power in the order of MW in the focus of the seed pulse, a fused silica glass pulse stretcher is positioned between seed and amplifier. The stretcher imprints a positive frequency chirp onto the laser pulse such that the peak intensity decreases below the damage threshold. A prism compressor after the amplifier compensates the imprinted chirp so that output laser pulse durations of sub 30 fs can be realized, see figure 3.1 c).

In order to get shorter pulse durations for efficient high harmonic generation the laser pulse is focused by a lens into a hollow-core fiber filled with 2 to 2.5 bar of Neon. Due to high laser intensities of about 10^{14} W/cm^2 inside the 1 m long capillary, self-phase modulation takes place. This modulation is based on the fact that the refractive index n of the used gas depends in second order on the light intensity $I(t)$: $n = n_0 + n_2 I(t)$. Thus, the refractive index increases in the leading edge of the light pulse and decreases again at the trailing edge making the refractive index time dependent. Because the index contributes directly to the phase ϕ of the electric field by $\phi = (k_0 nr - \omega t)$ the time-dependency adds new frequency components on top of the spectrum of the light pulse propagating through the fiber. In addition, several effects like HHG, multiwave mixing or cross-phase modulation contribute to new frequency components. A detailed description of these effects can be found e.g. in [34].

In order to avoid damage to the fiber by high peak powers at the fiber cladding the pointing of the laser is stabilized by a beam alignment system (by piezosystem jena, Inc.) with a beam pointing stabilizing mirror in the compressor and another in front of the hollow-core fiber. Due to propagation through the gas-filled fiber a nonlinear chirp is imprinted onto the laser pulse which is partly compensated by a chirped-mirror compressor and can be fine-tuned by two BK-7 glass wedges (figure 3.1 e)). The whole system is temperature and humidity stabilized, but it is still very sensitive and has therefore to be adjusted daily. With proper alignment it provides a laser pulse of 0.3 mJ pulse energy

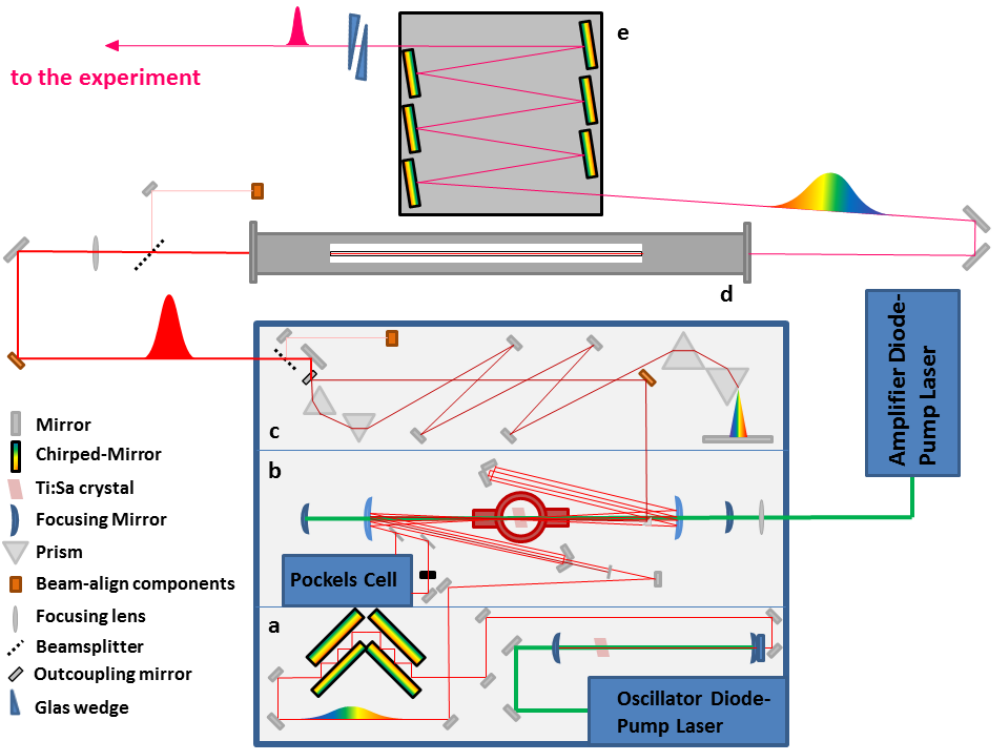

Figure 3.1: Sketch of the commercially available laser system, Femtopower compact Pro CEP by FEMTOLASERS Produktions GmbH. The CEP stabilization unit was not used and is not sketched. a) the 'Rainbow' oscillator with the pulse stretcher for chirped pulse amplification. b) 9-pass amplifier triggered by a pockels cell. c) prism compressor. d) hollow-core fiber for spectral broadening. e) chirped mirrors correcting the imprinted chirp onto the pulse together with two glass wedges for fine tuning. More details of the specifications are in the main text. The figure was adapted and modified from [33].

and pulse durations down to ∼5 fs FWHM measured by a home-built D-Scan setup [35].

3.2 XUV pulse production and NIR pulse manipulation

The laser pulse is then focused by a spherical mirror, 500 mm focal length, into a machine-drilled pinhole, 100 micron in diameter, of a gas filled stainless-steel tube producing high harmonics (HH), see figure 3.2 a). The conversion media are the backing pressure controlled rare gases argon or xenon, which have ionization potentials of 15.7 eV and 12.1 eV, respectively, whereby the latter was used for XUV spectroscopy in the 13 to 17 eV range investigated in this work. For better phase-matching conditions the cell can be translated along the optical axis and also perpendicular to that axis for adjustment purposes. Some side peaks in the nearly Gaussian beam profile of the laser pulses are blocked by an iris aperture in front of the focusing mirror. This manipulates the NIR beam wavefront which can further increase the high-harmonics production efficiency. Due to the short absorption length of the XUV light in air of less than 1 mm in the 20 eV range [36] the HH production and the further experimental setup is constructed inside vacuum chambers. All following mechanical parts need therefore to be controlled under vacuum conditions of about 10^{-8} mbar up to 10^{-3} mbar in the HHG and target chambers.

In the experiment a broadband XUV pulse produced by HHG and the fundamental NIR laser pulse are used for both time-delay and NIR-intensity-dependent transient absorption spectroscopy. The intensity of the NIR pulse is controlled by a closed-loop zero-aperture iris (figure 3.2 b)). The aperture blocks parts of the NIR light, whereby the copropagating XUV-pulse is almost not affected due to its smaller divergence of about 1 mrad compared to the 15 mrad NIR-divergence and [37].

The time delay is realized by a split-mirror in grazing incidence of 15° (figure 3.2 c)), where a 2 mm x 10 mm inner gold-coated mirror can be translated with nanometer precision by a piezoelectric stage perpendicular to the mirror surface with respect to a fixed outer silver-coated mirror yielding a possible

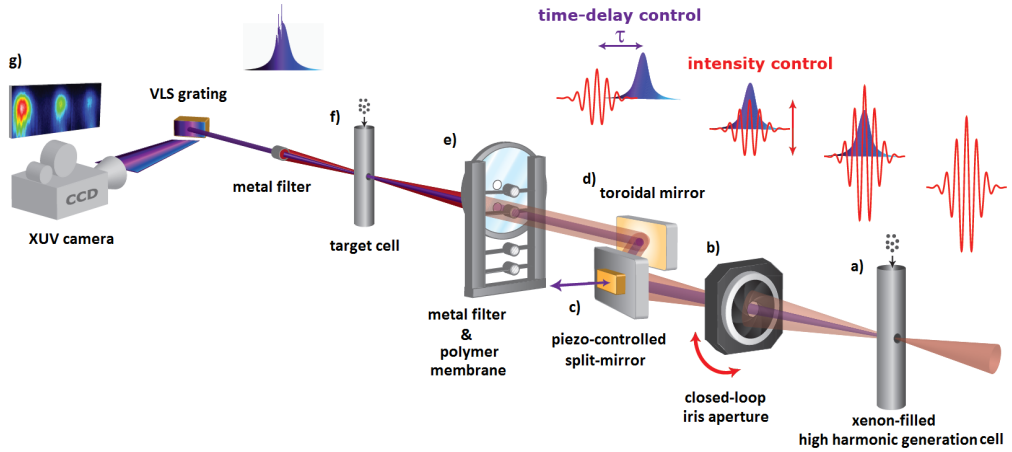

Figure 3.2: Sketch of the experimental setup for attosecond transient absorption spectroscopy. a) high-harmonic generation cell. b) closed-loop iris aperture, which blocks partly the NIR pulse and leaves the XUV pulse unaffected. c) split-mirror providing time-delay control between XUV and NIR pulse. d) toroidal mirror, which focuses both pulses into the target cell. e) first metallic and polymer filter for purpose of spacial separation of the XUV and NIR pulse. f) argon or nitrogen filled target cell. g) second metallic filter, which blocks the NIR in order to protect the spectrometer. h) spectrometer with variable lines grating and XUV sensitive CCD camera.

time delay resolution on the order of 10 as [31]. Although the total translation range of the piezo is 400 micron corresponding to a time delay rang of 684.6 fs, the experimentally accessible time-delay maximum is about 50 fs limited by walk-off of the XUV focus in the target. Due to the moving of the inner mirror the focal spot of the XUV in the target cell gets displaced compared to the NIR focus. The residual NIR light, which is also reflected by the inner mirror is blocked by a 2 mm in diameter, round, 200 nm thin metallic filter-foil by Lebow, Inc (figure 3.2 e)). Depending on the investigated photon energy two different foil species were used. An aluminum filter transmits 60% of the XUV light from 16 eV to 74.5 eV and an indium filter covers the more interesting transmission region from 12 eV to 16.5 eV. In this case the transmission is about 25% and the use of the indium filter becomes more challenging (figure 3.3). A concentric 2 micron thin nitrocellulose membrane blocks possible residual HH-light reflected from the outer mirror. This, together with the spilt-mirror

leads in total to a temporal and spatial separation of XUV and the fundamental NIR pulse. The filter foils can have characteristic microholes yielding to small leakage of NIR sitting on top of the XUV pulse. With the help of this effective third pulse one may observe dipole-forbidden states from the atomic/molecular ground state contributing to the wavepacket dynamics seen in the transient absorption spectrum, see e.g. [38].

After time-delay implementation, both light pulses are focused by a toroidal mirror in grazing incidence (figure 3.2 d)) into a pinhole of a stainless steel tube filled with the pressure controlled atomic or molecular gas target under investigation (figure 3.2 f)). The focal point of the NIR beam in the target is about 50 micron in diameter which leads to a peak intensity on the order of 10^{12} W/cm^2, whereby the XUV peak intensity is still in the perturbative regime. After passing the target, the strong NIR is filtered out by a second aluminum or indium filter protecting the subsequent spectrometer from stray light or damage (figure 3.2 g)). In order to minimize the leakage due to the microholes of the filter foils, a stack of two filters is used each with 5 mm in diameter and 200 nm thickness. Thus, the XUV pulse has to pass three metallic filters in total leading, in case of indium, to a total transmission of only 1.5% making the access of this small energy region very challenging. Using thinner filters e.g. with 0.1 nm thickness would therefore strongly increase the signal. However, they have proved to be very fragile and a successful measurement could not be performed yet. Provided that the filter foil absorbs the entire power P of the NIR-light which is, assuming a Gaussian pulse in time, with equation 2.5 roughly:

$$\begin{aligned} P = \nu_{rep}\epsilon = \nu_{rep}\frac{\pi}{1.88} I_{peak}\omega^2\tau \\ \approx 4\,\mathrm{kHz}\frac{\pi}{1.88} 5\cdot 10^2\,\mathrm{W/cm^2}\cdot(70\,\mu\mathrm{m})^2\cdot 7\,\mathrm{fs} \\ \approx 11.5\,\mathrm{mW}, \end{aligned} \tag{3.1}$$

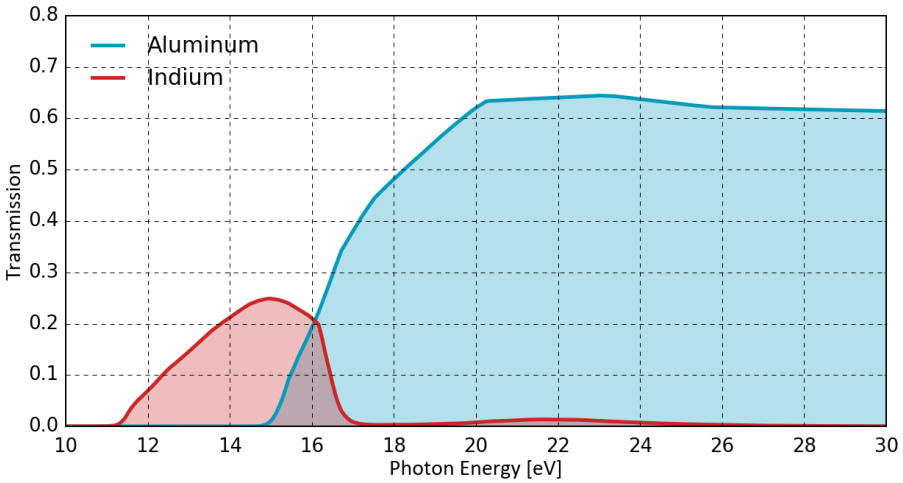

Figure 3.3: Transmission of a single 200 nm thin aluminum and indium filter in the spectral range between 10 and 30 eV. The transmission of aluminum reaches 60% from 20 eV to higher energies, but blocks almost all the light below 16 eV. The indium filter covers the lower energy region down to 12 eV, but with a maximum transmission of only 25%. The data are from [36].

further assuming the indium filter is a cylinder with cross section $2\pi r \cdot h = 2\pi r \cdot 100\,\text{nm}$, radius $r = 2.5\,\text{mm}$ and thermal conductivity of $\lambda = 82\,\text{W/mK}$ it will heat up to [39]

$$\begin{aligned} T &\approx P\frac{r}{\lambda \cdot h \cdot 2\pi r} + T_0 \\ &\approx 11.5\,\text{mW}\frac{2.5\,\text{mm}}{82\,\text{W/mK} \cdot 100\,\text{nm} \cdot 2.5\,\text{mm} \cdot 2\pi} + 295\,\text{K} \\ &\approx 518\,\text{K} \end{aligned} \tag{3.2}$$

which is above the indium melting point of 429.75 K [40]. Even with 200 nm thick filters the temperature is close to the melting point. Therefore a pinhole in front of the filter already blocks parts of the NIR intensity without affecting the XUV light due to its aforementioned smaller divergence.

3.3 High-resolution flat-field XUV spectrometer

In attosecond transient absorption spectroscopy the measured quantity is the optical density of the target medium, which is accessed in our experiment by measuring the XUV-intensity spectrum with and without target by a grating and a charge-coupled device (CCD)-camera. Our grating by Hitachi, Ltd. Corporation is an aberration-corrected concave grating with a variable groove density or also called variable line space grating (VLS) providing a flat-field spectroscopic image rather than an image on a Rowland circle generated by conventional gratings, see figure 3.4, [41]. Thus, the spectrum can be recorded by a usual flat camera chip with low distortion. For energies from 10 eV to 100 eV, which are interesting in atomic and molecular spectroscopy Hitachi provides two similar gold-coated pyrex VLS-gratings, one with 1200 averaged grooves per mm for wavelengths from 11 to 62 nm corresponding to about 20 to 112 eV photon energy and a second with 600 grooves per mm for 22 to 124 nm wavelength corresponding to 10 to 56 eV [42]. In order to cover the entire energy range in a single experimental setup a new grating holder was designed within this master thesis allowing to switch between these two gratings under vacuum conditions with low effort (figure 3.5). The gratings are mounted individually on ultra-stable mirror mounts (POLARIS by Thorlabs, Inc.) providing full access for tilting, positioning and rotating. Thereby, both gratings can be tuned separately to high diffraction efficiency and resolution. The mirror mounts are fixed on an H-shaped holder, which can be lifted by a crank-driven linear-feedthrough and is guided by rails for mechanical stability. In addition a silica plate can also be mounted on the grating holder reflecting the zero order of the XUV light onto the camera which can be used for adjustment purposes. The spectrum is recorded by a back-illuminated thermo-electrically cooled CCD with 1340x400 Pixels by Princeton Instruments, which can be translated along the flat-field spectrum stabilized by a home-build stage for better reproducibility.

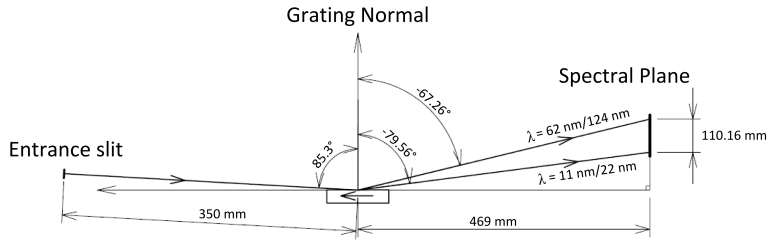

Figure 3.4: Sketch of the aberration-corrected concave grating with a variable groove density by Hitachi, Ltd. Corporation. It is also called variable line space grating (VLS). The spectral image is created on a flat plane rather than on a Rowland circle known from conventional gratings [41]. Two gratings are used in the experiment with different averaged groove density covering certain wavelength regions. The geometrical conditions depicted here have to be fulfilled in the setup to get the best diffraction efficiency and wavelength resolution. The figure is adapted from [42].

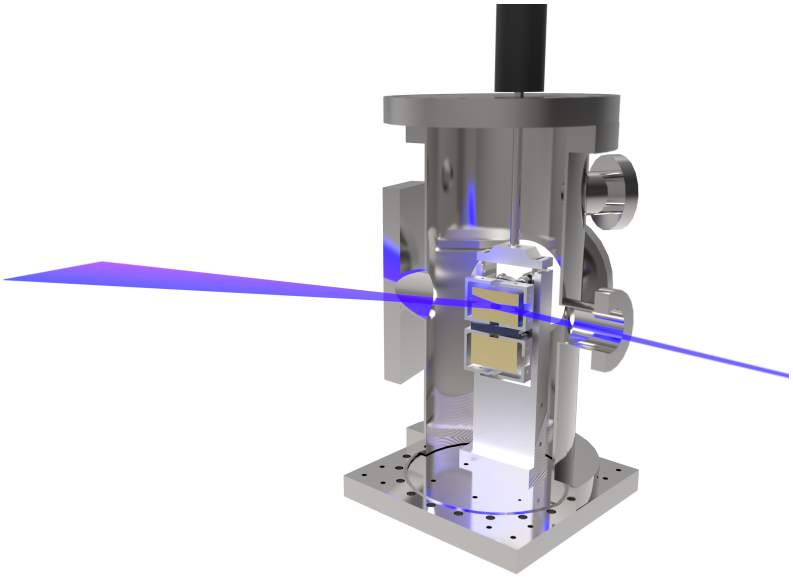

Figure 3.5: Design of the new home-build grating holder allowing to switch between the two gratings under vacuum conditions with low effort. The position and angle of both gratings can be adjusted separately for better diffraction efficiency and resolution. In addition a silica plate can be mounted between the gratings reflecting the zero order of the XUV onto the camera for adjustment purposes.

4 Data Acquisition and Calibration

In this work the optical densities of argon and molecular nitrogen are recorded for the direct comparison of atomic and molecular systems in transient absorption spectroscopy. The shared energy region close to the first ionization threshold of both species between 13 and 17 eV with respect to the ground states is of key interest. This becomes accessible with the help of the new grating setup and indium filters presented in the previous chapter. The current chapter gives an overview of the data acquisition and calibration procedures including the most important details about the elaborated methods. Since the work presented here is the first benchmark experiment on molecules in this research group the section serves also as a reference for future experiments. The presentation and interpretation of the recorded data is given in the next chapter. Due to the low transmission of the indium filter of only 1.5% in total, long data acquisition times were needed. Thus, the total recording was divided into two modes. One focuses on long time delays with coarse intensity steps and the second mode was carried out with fine intensity steps but short time-delay ranges. The reference spectrum for the determination of the optical density was retrieved by Fourier-filter methods. Its reconstruction is explained along with a data smoothing procedure at the end of this chapter. The examples here are all for argon, but all these methods also apply to nitrogen.

4.1 Time-delay scans

In the long time-delay scans the position of the inner-mirror piezo was randomly scanned with 0.1 micron step size corresponding to 0.171 fs time-delay resolution [31]. The randomness of the inner-mirror position averages the long oscillatory laser drifts, which occur due to the long camera integration times of 10 seconds for argon and 7 seconds for nitrogen per time-delay step. The scans were performed for split-mirror piezo-positions from 140 to 180 micron for argon and 138 to 168 micron for nitrogen. This corresponds to time-delay ranges

from ∼-7.7 to ∼60.7 fs and ∼-11.1 to ∼40.2 fs, respectively calibrated with the procedure below. Negative time-delay means the NIR pulse comes before the XUV pulse and thus, the ranges cover the whole pulse overlap and some region where the NIR pulse manipulates the target after the XUV-excitation step. The total recording time, which includes the absorption data as well as the reference data takes therefore more than 10 hours. For the duration of this measurement time the laser together with the nonlinear HHG production has to be stabilized.

The camera records the absorption spectrum by binning the signal automatically in the vertical direction preserving the horizontal wavelength information. This yields a faster camera acquisition compared to taking full chip images. High harmonics were produced in xenon gas at a backing pressure of 35 mbar and the HHG capillary was driven to a position about 5 cm behind the NIR focus both to achieve the best phase-matching condition and thereby maximizing the intensity of the harmonics in the studied energy range. The target backing pressure of 13 mbar for argon and 5 mbar for nitrogen were adjusted for high absorption-line visibility without total light absorption in the energy range of the continuum of single ionization. The time-delay spectra were recorded for five iris aperture positions and hence five NIR intensities yielding scans starting at hardly any NIR light to intensities which ionize almost the complete target. The NIR input powers were 885 mW for argon and 600 mW for nitrogen measured directly in front of the vacuum chambers.

4.2 Intensity scans

The intensity scan was recorded under a similar HHG, NIR and camera setup as in the aforementioned time-delay scans, but here the NIR intensity was finely scanned in 10 steps at an input power of 920 mW. However, the inner-mirror piezo-position range was smaller from 146 to 152 micron corresponding to ∼2.5 to ∼12.8 fs and hence only positive time delays. This range covers the region where the whole NIR pulse comes after the XUV excitation and thus affects the target maximally after excitation. For better comparison of the intensity dependency the target gas was switched between argon and nitrogen within every single intensity step. The target backing pressure was 10.2 mbar for argon and 4.6 mbar for nitrogen and the camera integration time was 7 seconds per time-delay step. In the intensity-dependent spectra the recorded data is

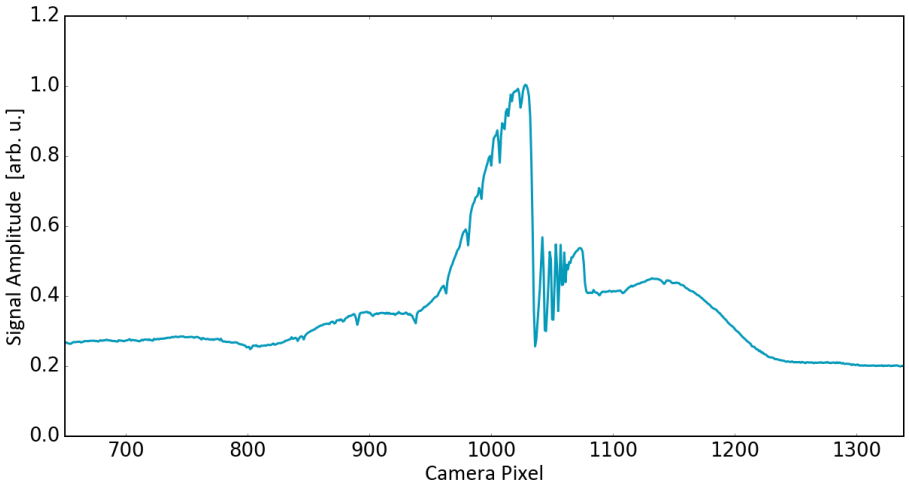

Figure 4.1: Example of an absorption spectrum in argon without NIR. The sharp edge points to the first ionization threshold. Rydberg series are visible for lower and greater pixel positions. For better visibility the signal is integrated over the whole time delay.

averaged over one full electric-field cycle of the NIR of ∼2.5 fs at the central time delay of 5 fs smearing out sub-cycle effects of the dressing electric field on the shape of the absorption lines.

4.3 Photon energy axis calibration

The grating maps the photon wavelength onto a horizontal line on the recording camera. For the calibration of the a photon-energy axis, the relationship $h\nu = hc/\lambda$ between photon energy $h\nu$, speed of light c and wavelength λ and the corresponding derivative $|\frac{d(h\nu)}{d\lambda}| = \frac{hc}{\lambda^2}$ was used in a polynomial fit through known absorption energies in argon or nitrogen and camera pixels. For the first determination of absorption lines - seen as Rydberg series up to different ionization thresholds e.g. in argon (figure 4.1) - the well-known window resonances in argon were recorded. These readily distinguishable resonances lie at 26.606 eV for principal quantum number n = 4 up to 28.898 eV for n = 8, see figure 4.2 [43]. Thus, their spectrum overlaps in second diffraction order with the investigated spectra and it can be separately recorded with the help of the aluminum filters. Using these resonances for the calibration gives good agree-

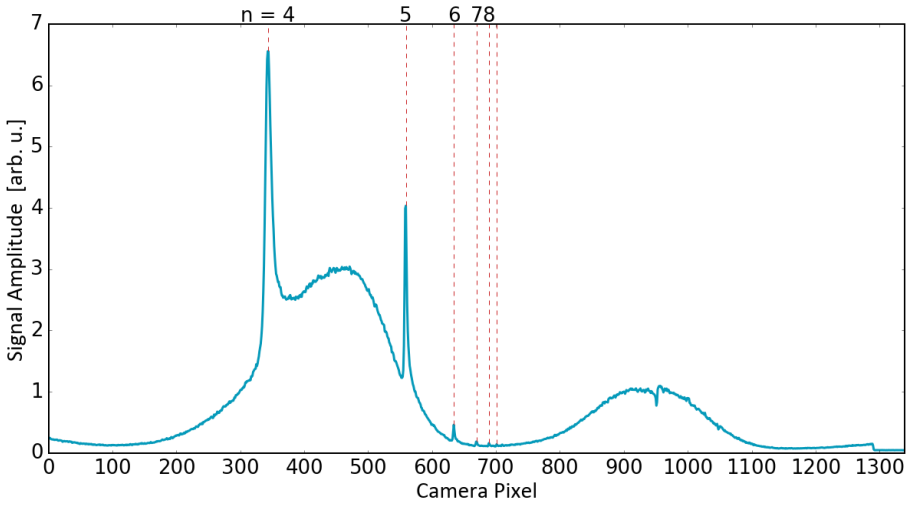

Figure 4.2: Window resonances in argon between 26 and 29 eV sitting on top of the left harmonic modulation. Dotted lines indicate the line positions. These resonances are clearly visible in second diffraction order with the help of the aluminum that transmits this energy range and blocks the first order.

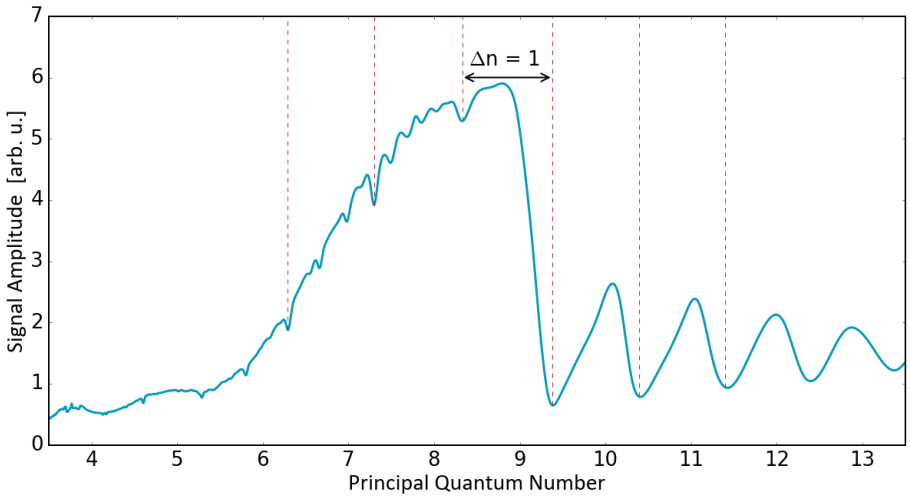

Figure 4.3: Resampled absorption spectrum in argon from figure 4.1 against the principal quantum number $n = \sqrt{I_p/(I_p\text{-}E)}$ with $I_p = 15.96$ eV. Absorption lines belonging to the same Rydberg series converging to I_p are equidistant with distance one.

ment for energy positions of the states found in literature [44] and the observed photon energies only between 13 and 15 eV. However, the calibration still has an energy distortion for lower and higher lying lines. In order to uncover the assignment of the Rydberg series for the entire spectral range the roughly energy-calibrated spectrum can be resampled versus $\sqrt{I_p/(I_p\text{-}E)}$ where I_p is some ionization energy. Here the absorption lines corresponding to a Rydberg series converging to I_p are aligned with distance 1 in the resampled spectrum and they are therefore easy to assign (figure 4.3). Assuming that only first-order dipole-allowed absorption lines in atomic argon with odd parity and unity total electronic angular momentum are visible, the lines with energies above the first ionization threshold of 15.76 eV can be identified as the $3s^2 3p^5(^2P_{1/2})$ns/d Rydberg series starting with n = 11. One can use these states together with the window resonances to calibrate the energy axis adequately for both species. An extensive level mapping is presented in the next chapter, see figure 5.1 and 5.5.

4.4 Time-delay axis calibration

In order to calibrate the time-delay axis, the time overlap of two NIR-pulses reflected by the inner and outer-mirror was investigated in an individual calibration procedure. The point at zero time-delay of the split-mirror was set to the position $\sim$146.5 micron, where the maximal beating of the interference fringes of both pulses was visible with the help of a beam-profile camera. In the experiment the filter for NIR and XUV-beam separation is mounted in the light path introducing an additional delay. Whereas the influence of the 200 nm thin metallic filter is negligible, one has to take into account the delay due to the nitrocellulose membrane. It has a refractive index of about 1.5 [45] and a thickness of 2 μm leading to an approximate propagation delay of 3.3 fs for the NIR. Considering the geometry of the split-mirror setup the translation of the inner-mirror introduces a time delay of 1.7115 fs per micron [31]. Thus, the approximate zero position is at about 144.5$\pm$0.5 micron inner mirror position, with a precision that is sufficient for this work. For a better determination of the zero time-delay position an attosecond streaking camera, which trace the electric field of the pulses, will be implemented in the experimental setup in the future [46].

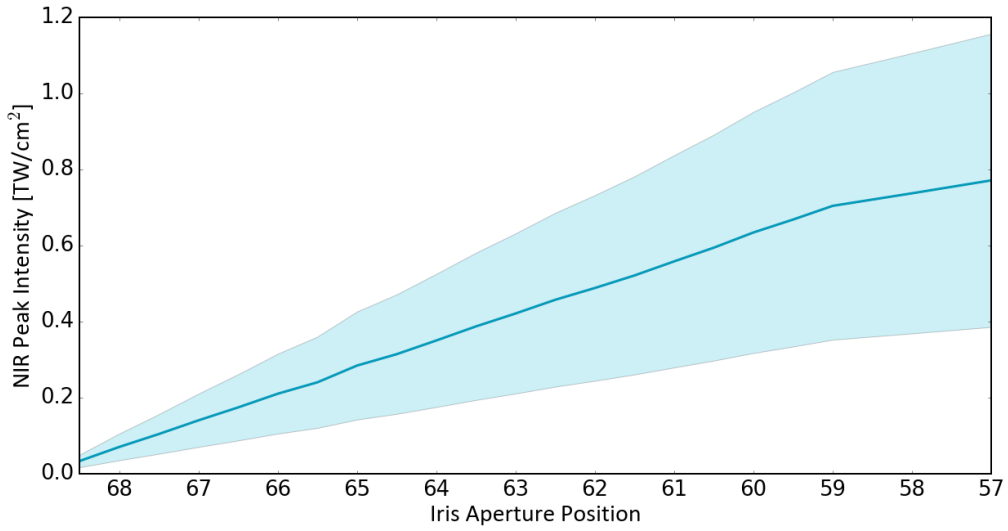

Figure 4.4: The mapping between the NIR peak intensity in the target and the iris opening positions for an input power of 900 W/cm^2. The dependency is almost linear in the region considered in this work. The position 70 means the iris is closed where at position 50 the iris does not block any NIR. The shaded area indicates the error of 50% in the NIR peak intensity.

4.5 Intensity calibration

For the intensity-axis calibration the Autler-Townes splitting of the 2s2p and 2p^2 states in helium were compared between an experiment with conditions similar to this work and a simulation for different NIR intensities and durations [31, 37]. This splitting is dependent on the NIR intensity, which increases, when the iris aperture opens up. The mapping of the intensity and the iris opening position is depicted in figure 4.4. The data has a systematic uncertainty of 50% mainly due to uncertainties in the pulse duration and in the time delay between the XUV and NIR pulses.

4.6 Reference spectrum

An example of a harmonic reference spectrum together with an absorption spectrum in argon is depicted in figure 4.5. Due to the high-order nonlinear process of high-harmonic generation the reference spectrum differs slightly

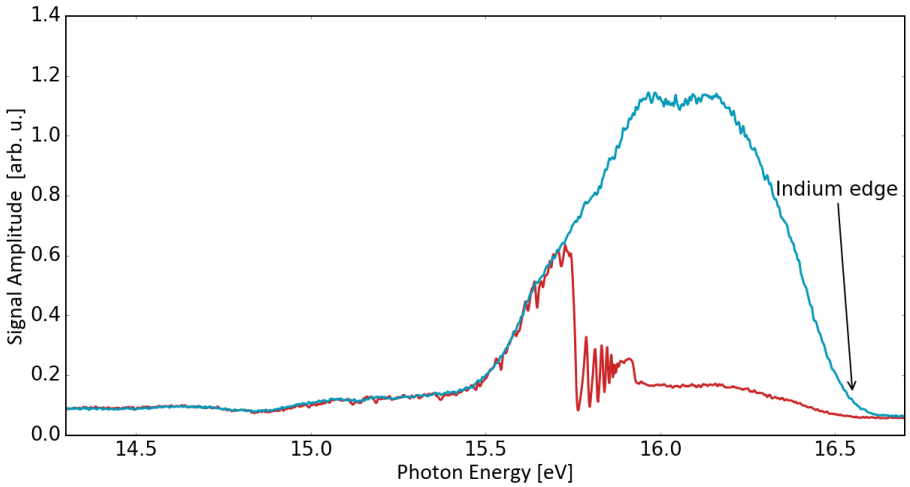

Figure 4.5: Example of a reference spectrum in the argon time-delay scan in blue. Only a narrow energy range is transmitted trough the indium filter. On the right, one can see the indium edge absorbing all the light. The corresponding absorption spectrum in argon is drawn in red.

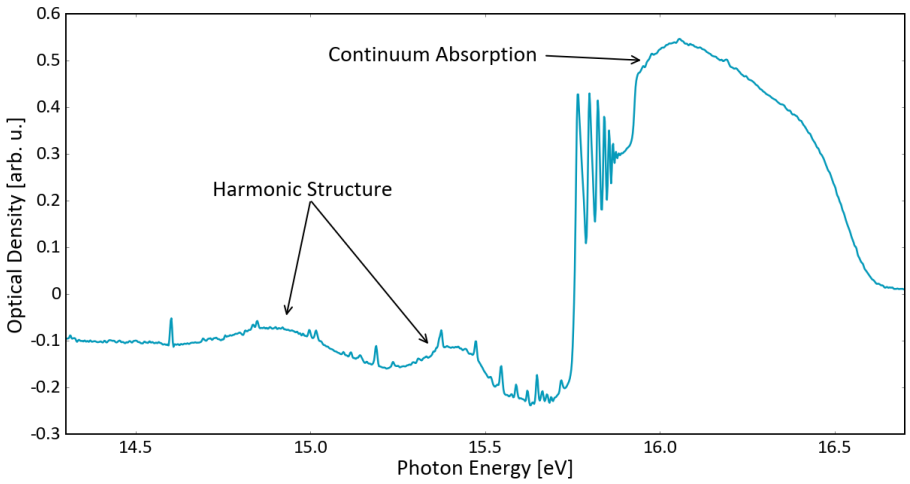

Figure 4.6: Optical density calculated by the reference spectrum in figure 4.5. Harmonic structure still appears together with a broad signature in the continuum absorption range. For different time delays these structures look different due to the harmonic fluctuations shot by shot. Thus, in the time-delay scan a modulation based in this variation will be visible, which makes it hard to accurately determine the time-delay or intensity-dependent change in the absorption line.

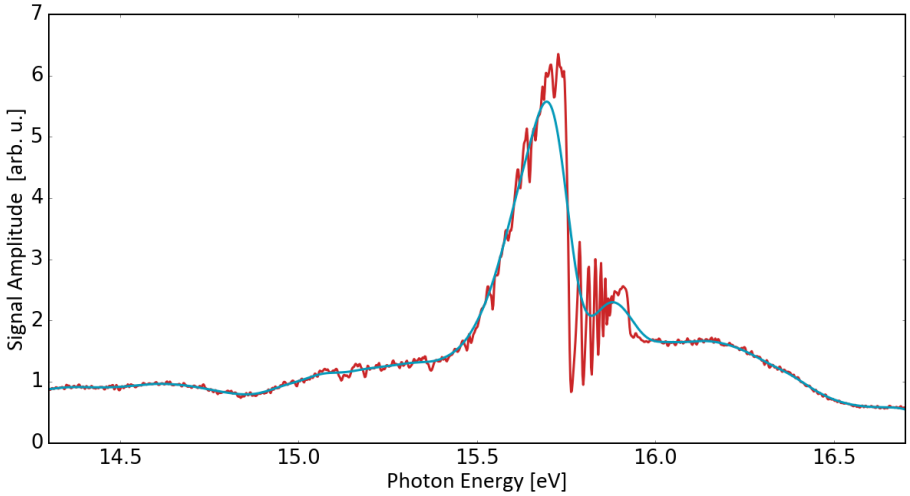

Figure 4.7: Reference spectrum by Fourier filter method (blue) and the absorption spectrum in argon (red). The sharp absorption lines disappear leaving the smooth harmonics modulation unaffected. However, close to the ionization threshold the Fourier reference does not follow the correct modulations, which leads to Fourier overshoots in the retrieved optical density.

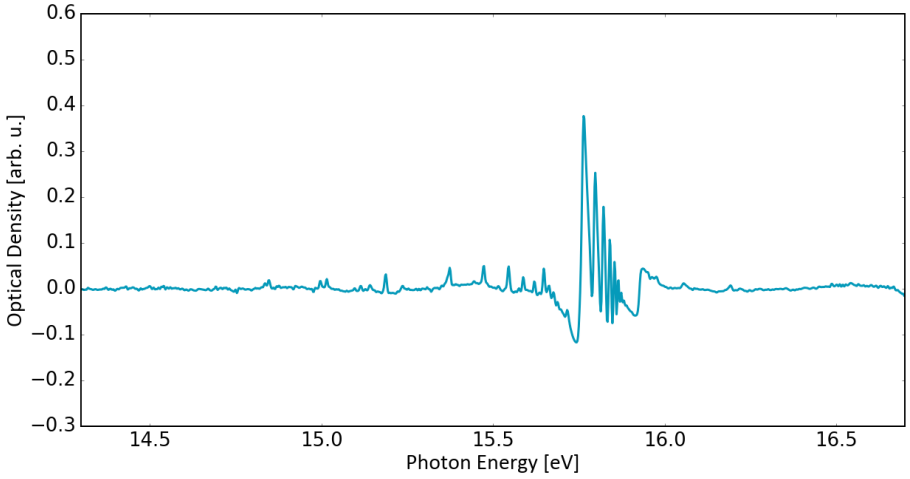

Figure 4.8: Optical density calculated by the Fourier reference spectrum in figure 4.7. The harmonic modulation, the broad continuum signature and the non-resonant absorption disappear. This kind of figure makes it easy to determine changes in time- or intensity-dependent absorption lines due to the reproducibility of the reference spectrum.

from shot to shot caused by unavoidable fluctuations of the beam pointing and the intensity of the fundamental laser. As a result a proper calculation of the optical density fails due to residual harmonic fringes even for long integration times (figure 4.6). To overcome this issue one may record the reference spectrum simultaneously to the absorption data. However, this was not possible in the available setup. Here part of the signal itself is used for the reference and it is exploited that the absorption lines are very sharp compared to the harmonic modulation. If the signal is Fourier transformed along the energy axis and filtered by a low-pass $\cos^2$-filter function it will maintain only low frequency components. After inverse Fourier transformation the spectrum shows only the harmonic structure without the sharp absorption features, see figure 4.7. In using this reference spectrum for optical-density calculations the harmonic modulation vanishes but also the non-resonant absorption contributions (figure 4.8). Thus, not the absolute optical density but its changes are visible by this filter method, which is sufficient in this work because only the time-delay or intensity-dependent changes in the absorption lines are of interest. In order to get the right optical density in addition one has to correct the Fourier reference according to the Lambert Beer's law by the factor $\exp(\sigma(\omega) \cdot \rho \cdot l)$, where $\sigma(\omega)$ is the photon-energy-dependent non-resonant absorption cross-section, ρ the gas density and l the propagation length. However, this correction gives only an energy-dependent offset to the optical density and is therefore omitted in the presented data.

The choice of the low-pass filter range and the smoothness at the filter-edges are crucial in order to ensure the correct vanishing of the harmonic modulation without affecting the absorption line signal too much. If the filter edges are too sharp one will get an artificial overshooting signal for the optical density. Thus, one has to choose the filter edges as smooth as possible. But this leads to a longer filter width, so that at some point the absorption signals start to decrease. Figure 4.9 shows the dependency of the optical density on the smoothness (in Filter width) of the filter edges. In the following discussion we choose the length of 60 for the data array of the filter function as the best compromise between vanished harmonic modulation and maximal signal.

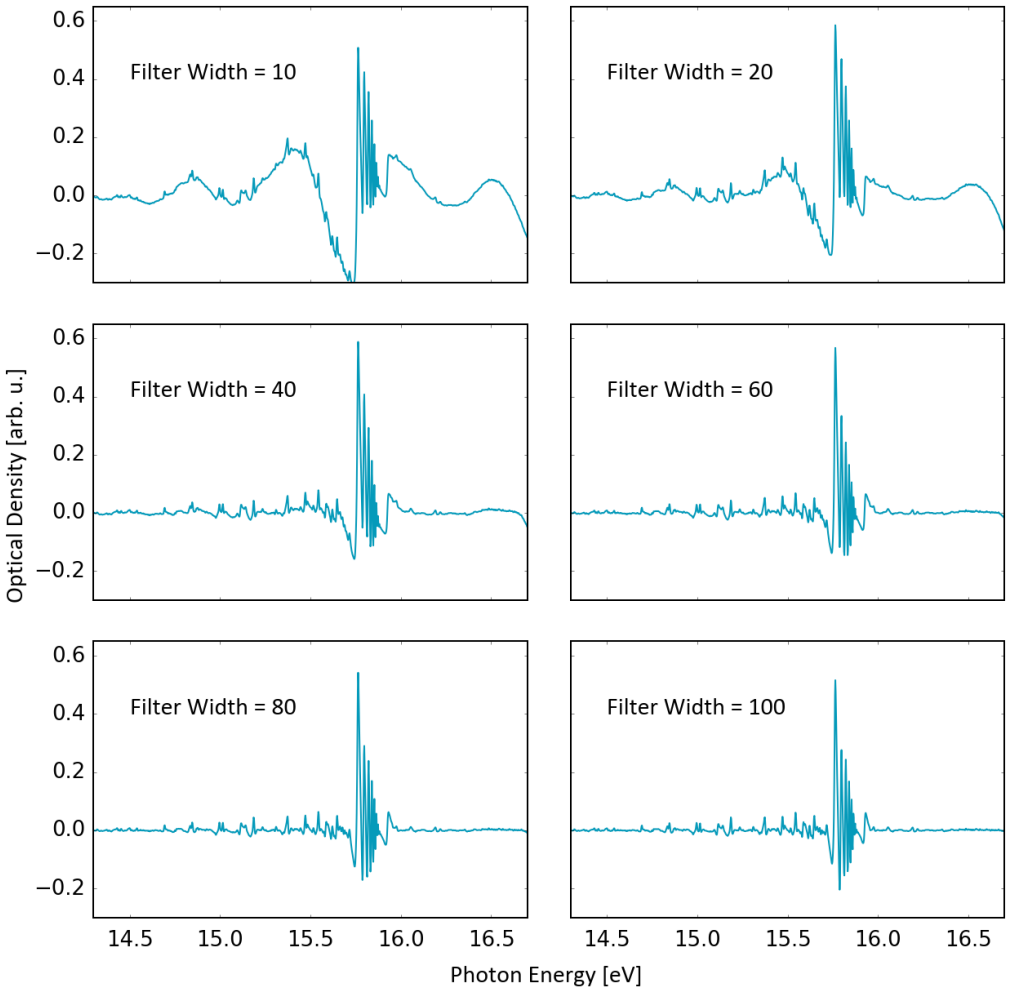

Figure 4.9: Optical density calculated by Fourier-reference spectra for different width of the $\cos^2$-filter functions in data-array length. For a small width only low Fourier components next to the DC peak are selected for the Fourier reference leading to an optical density which has still an appearing harmonic modulation. By increasing the filter-width also more Fourier components contribute to the reference spectrum smoothing the optical density and leaving the sharp absorption lines unaffected. For long width the signal starts to decrease. The best signal is obtained with the filter width = 60, which is is used in the following discussion.

4.7 Hot pixel removal

The long integration times in the order of seconds for the data acquisition of a single time-delay step increase the chance for cosmic rays to hit the camera producing high signals at certain pixels. These show up like hot pixels in the time-delay scans and produce artificial Fourier components in the two-dimensional Fourier plots. They are seen as continuous lines along the Fourier energy axis overlapping with the real signal, see figure 4.10 on the left. The hot pixels are localized with high probability at only one data point along the time-delay axis. Replacing the hot pixels by the average signal of one time-delay step back and forth of the same photon energy minimizes this artifact with very little modification of the physical information, see figure 4.10 on the right. In order to find the proper peak positions in a systematic way the second derivative along the time-delay axis is taken of the whole spectrum. Because this derivative is greater at these peak positions than everything else caused by physical effects, they can be easily identified. Even though many artificial components vanish, this procedure is not perfect and one still has to be careful in declaring new physics seen in particular in the two-dimensional Fourier plots.

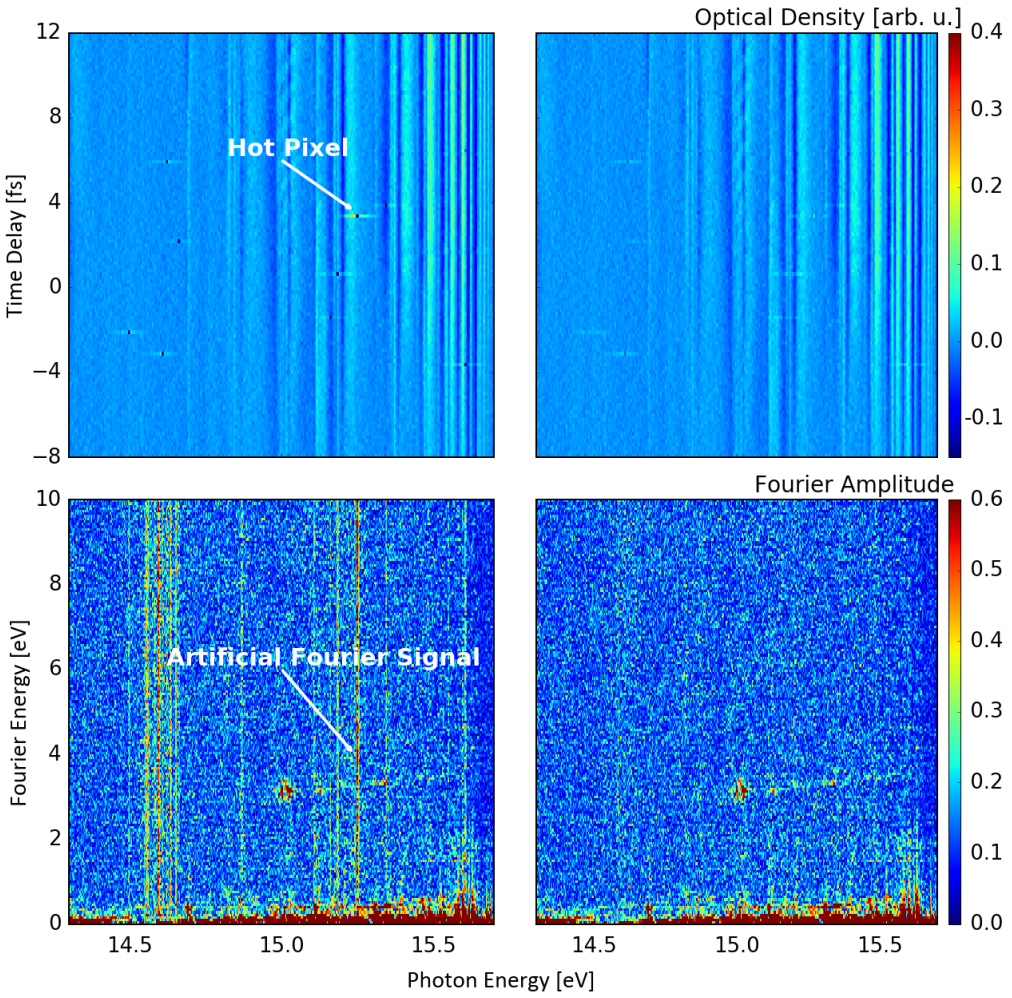

Figure 4.10: Time-delay scan and corresponding Fourier spectrum along the time-delay axis in argon. On the left the hot pixels produced by cosmic rays in the time-delay scan lead to artificial continuous components in the Fourier spectrum. These components overlap with the real physical signal and by systematically removing the hot pixels the real signal is more clearly visible, on the right.

5 Measurement Results

Many scientific papers or theses about attosecond transient absorption spectroscopy (ATAS) state in their outlook the scientific goal to do experiments in more complex systems like molecules or solids, see e.g. [27, 31, 37, 38, 47]. The hope is, among other things, to gain insight into the charge migration and molecule dissociation in such systems. This work represents one step towards this goal. The following chapter discusses the first ATAS experiment in molecular nitrogen with a tunable NIR-Peak intensity and thereby serves as our first benchmark experiment on molecules. The first part treats the time-delay scans in argon and nitrogen for some fixed NIR intensities. Here, one can directly compare the behavior of atomic and diatomic molecular systems in ATAS experiments at a common energy. A beneficial tool for the evaluation of the time-delay dependent data in ATAS is to analyze dynamical contributions by Fourier transformation along the time-delay axis [29]. With this method, one can map periodic modulations in the optical density, which originate from population transfers of quantum mechanical states, onto the corresponding Fourier energy. The location of a maximum in Fourier amplitude indicates the energy differences of the states that are involved in the corresponding transition. The second part investigates the intensity dependency of the optical density in direct comparison of atomic and molecular systems. In particular, the changes in the absorption line shape and their corresponding laser-imposed phases on the time-dependent dipole moment are of interest.

5.1 Time-delay scans

Complete scans of the time-delay dependent optical density and the corresponding Fourier spectrum are shown in figure 5.1 for argon and in figure 5.5 for molecular nitrogen. The assignments of the absorption lines to the corresponding quantum stats are depicted below both scans. For this, benchmark synchrotron data was taken from reference [44] for argon. The quantum state

assignment in nitrogen is controversial in the literature, making a clear mapping between absorption lines and the corresponding transitions difficult, see e.g. [48–54]. For this work, the assignment from the comprehensive overview by Lofthus et al. [55] was taken, which associates the lines below the first ionization threshold with the c_n states of $^1\Pi_u$ symmetry. For higher lying states, the elaborate interpretations by Lefebvre-Brion are used covering the series converging to the $A^2\Pi_u$ N_2^+ ionic core [50]. These assignments give interpretations of most of the lines seen in the spectra. However, due to the still ongoing debate, the question of the exact assignment remains open.

The discussion first covers the effects in argon as a (simple) atomic system. Here, many effects are already known from previous experiments e.g. in helium [5] or neon [56]. Afterwards, the time-delay scan in nitrogen will be introduced where similar, atomic-like behaviors are visible. However, due to the vibronic and rotational energy structure also uniquely molecular effects are arise.

5.1.1 Time-delay scan in argon

The electronic configuration of the argon ground state with zero energy is $1s^2\ 2s^2\ 2p^6\ 3s^2\ 3p^6$. Accordingly, there are four dipole-allowed Rydberg series visible, namely the $3s^2 3p^5(^2P^o_{1/2\ /\ 3/2})$ns/d argon states, which converge to two different ionization thresholds at $I_{p\ 3/2} = 15.76$ eV and $I_{p\ 1/2} = 15.94$ eV with the total electronic angular momentum quantum number $J = 3/2$ or $1/2$ of the residual ion core. For these states, various effects of light-matter interaction are visible like line broadening, sideband structures, sub-cycle and slower modulations. The line broadening seen e.g. at marker 1 and the sideband structures e.g. at marker 2 in figure 5.1 were already seen in various species like in helium [5] or also very recently in argon in this energy region [57]. They can both be explained by the ac Stark shift of these states imposed by the strong NIR pulse.

The sub-cycle modulations were recognized to be based on population transfers between excited states induced by two NIR photons at positive time delays. In the presented measurement, one can clearly see for example a ∼1.3 fs oscillation of the optical density in the time-delay spectrum in the region of 15 eV photon energy, see marker 3 in figure 5.1 and figure 5.2 for an enhanced view. This oscillation leads to a Fourier peak at ∼3.1 eV in the corresponding Fourier spectrum. The NIR spectrum spans 300 nm at 750 nm central wavelength corre-

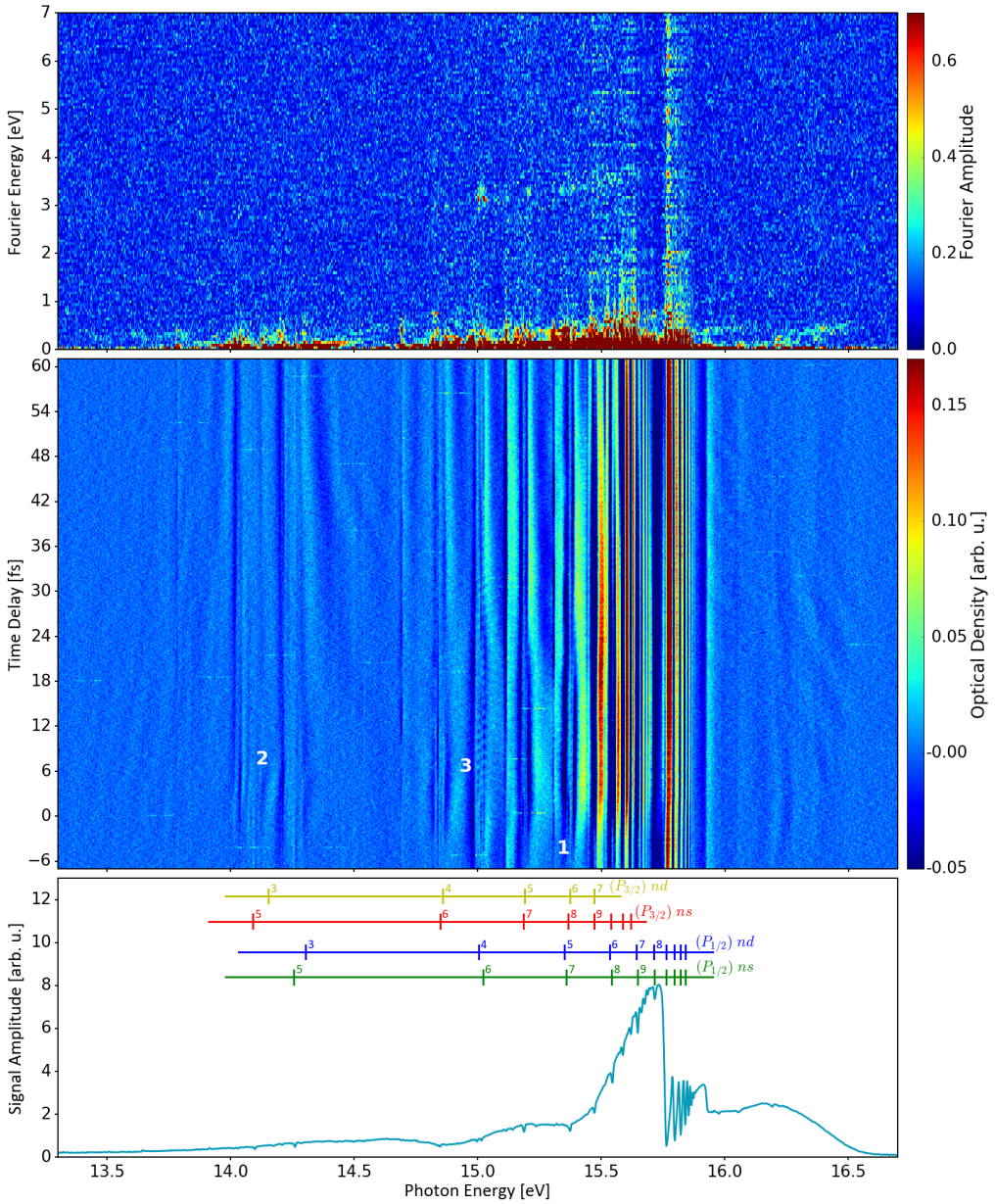

Figure 5.1: The time-delay dependent spectra in argon in the middle and the Fourier spectrum along the time-delay axis on top. Negative time delay means the XUV pulse arrives before the NIR pulse. The NIR peak intensity was ~3.4 TW/cm^2. Below an absorption spectrum is shown together with the assignment of the states, taken from reference [44]. For the marked effects seen in the time-delay spectra, see the explanation in the main text.

sponding to photon energies between 1.3 and 2.1 eV. Thus, the peak at ∼3.1 eV is probably a two-NIR-photon transition. The bright ($^2P_{1/2}$) 4s state of argon has the energy of 11.83 eV, ∼3.2 eV below the considered region. It is therefore a very good candidate to be involved in the two-photon coupling. One should in principle also see a modulation at this energy, but the signal below 13 eV was too low to obtain reasonable results. The transition is of ladder type and if it is mediated by an additional dark state lying between the two bright states, the signal will be enhanced. By looking for dark states, the 4p states around 13.3 eV are good candidates participating in this transition. Figure 5.2 b) shows a level diagram labeling the possible transitions.

A second interesting feature is the oscillation of the optical density in the continuum above both ionization thresholds at about 16.4 eV with a period of ∼10 fs (figure 5.3). Correspondingly, one can see a signal at about 400 meV Fourier energy in the Fourier spectrum. This oscillation probably indicates a Raman transition which is meditated by the continuum. The optical densities of the ($^2P_{3/2}$) 4d state at ∼14.7 eV and the ($^2P_{1/2}$) 6s/4d states at ∼15 eV and thus, one NIR-photon energy below the 16.4 eV, show a similar 10 fs oscillation (figures 5.4). They are probably involved in this transition, but it is not clear by now if the coupling is between these state or to a different third state. Because the Fourier energy of 400 meV corresponds to the energy differences of the states that are involved in the Raman transition, there are many other possible coupling partners. However, an oscillation of 10 fs in this time region could not be resolved for a different state yet.

5.1.2 Time-delay scan in nitrogen

The investigated energy range between 13 and 17 eV covers the nitrogen states converging to the first two ionization thresholds of the N_2^+ $X^2\Sigma_u^+$ and the N_2^+ $A^2\Pi_u$ ionic core. There are primarily two sets of Rydberg series. One is the c state with $^1\Pi_u$ symmetry below the first ionization threshold. Here, due to the Franck-Condon overlap the states with the vibronic quantum number $\nu = 0$ are mainly visible [55]. The second series belongs to the Rydberg states where one electron is excited to the molecular orbitals ndδ or ndσ. Here, vibronic states with $\nu = 0$ to states with $\nu = 3$ are visible. They all converge to the $A^2\Pi_u$ N_2^+ molecular ion.

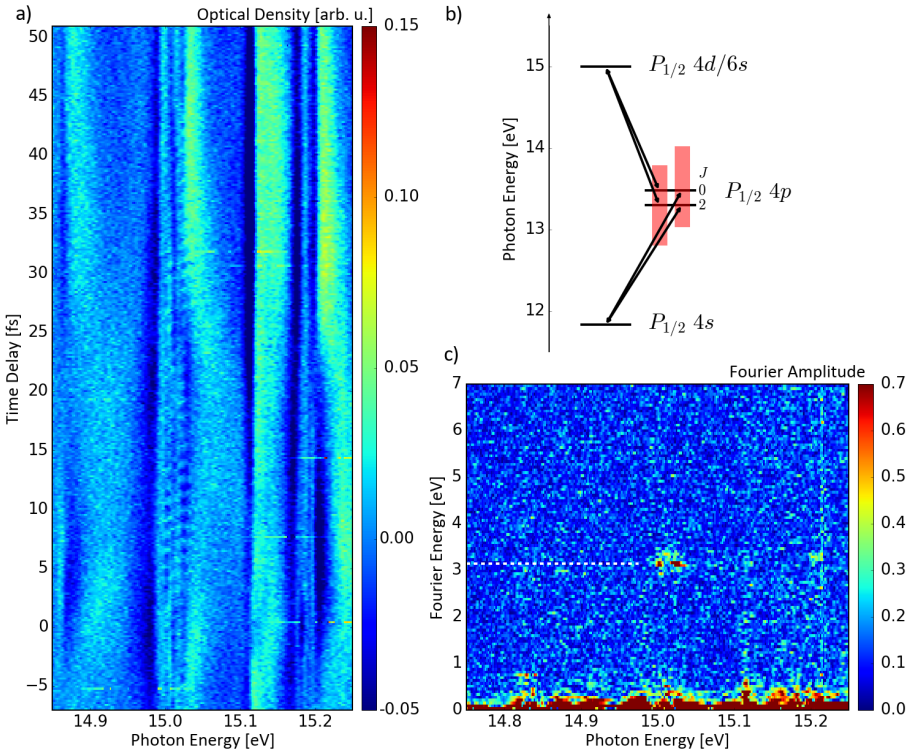

Figure 5.2: The sub-cycle modulation of the optical density of the $P_{1/2}$ 4d/6s states in argon. a) enhanced view of the time-delay dependent spectrum. A clear modulation at ∼15 eV is visible. b) the level diagram with a possible two photon transition between the $P_{1/2}$ 4d/6s and the $P_{1/2}$ 4s state marked with arrows. The red shadows indicate the bandwidth of the NIR pulse, which can in principle be reached with one photon. Both 4p states are in this region making them good candidates for mediating this transition. c) the Fourier spectrum at the considered photon energy. At 3.1 eV Fourier energy indicated by the white dotted line a Fourier amplitude is clearly visible. This corresponds to modulations of 1.3 fs in the time-delay spectrum.

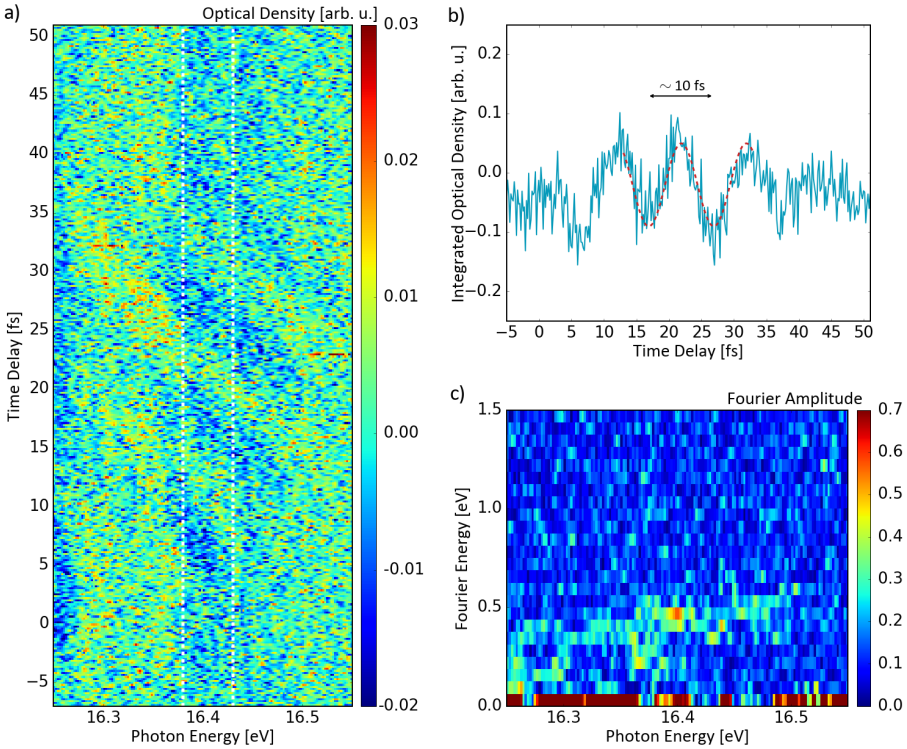

Figure 5.3: Optical-density modulation in the continuum energy range in argon. a) enhanced view of the time-delay dependent spectrum from 5.1. b) optical density lineout versus the time delay. The signal is integrated for better visibility along the photon energy between the dotted lines in the time-delay spectrum. A modulation of ∼10 fs is clearly visible. The red-dotted line is a sinusoidal curve with a period of 10 fs and serves as a guide to the eye. c) the corresponding Fourier spectrum at the considered energy. A Fourier peak at 400 meV according to the 10 fs modulation is visible.

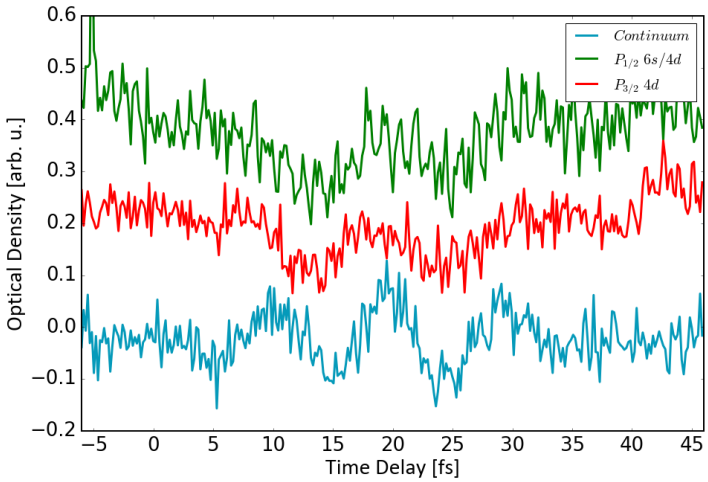

Figure 5.4: The oscillations of the optical densities in the continuum, the same as in figure 5.3 b), and of the $P_{1/2}$ 6s/4d at ∼15 eV and $P_{3/2}$ 4d states at ∼14.7 eV versus the time delay. For better visibility the signal is integrated along a small energy window around the states and shifted in optical density. All three lineouts show similar 10 fs modulations, which gives an indication that the states are probably involved in a Raman-type transition.

In the time-delay scan, the optical densities of these states show many similar signatures compared to the atomic case despite the two-nuclei structure of the molecule, which was also observed in a recent study by E. Warrick et al. [14]. For example, changes in the absorption line shape with respect to the time delay and even line inversion is visible, see marker 1 in figure 5.5. Furthermore sub-cycle modulations are present. For example the 1.3 fs modulation of the A 3dσ(2), A 3dδ(3) and A 4dδ(0) states in the region of 15.9 eV indicates two NIR-photon couplings to different states, see marker 2 in figure 5.5. One can see corresponding peaks of the Fourier amplitude in the range around 3.1 eV Fourier energy, see marker 3. In addition, a broad signal at 1.6 eV Fourier energy is visible caused by full-cycle modulations in the time delay scan. This indicates strong one-photon couplings, which are greater than in the atomic case. Furthermore, also slower modulations are present. For example, the A 4/5/7dσ(0/1/2) states at about 16.45 eV have an indication for a ∼20 fs modulation, see marker 4. This should correspond to a Fourier energy of 200 meV and it might be a v-type or λ-type coupling. However, this cannot be resolved in

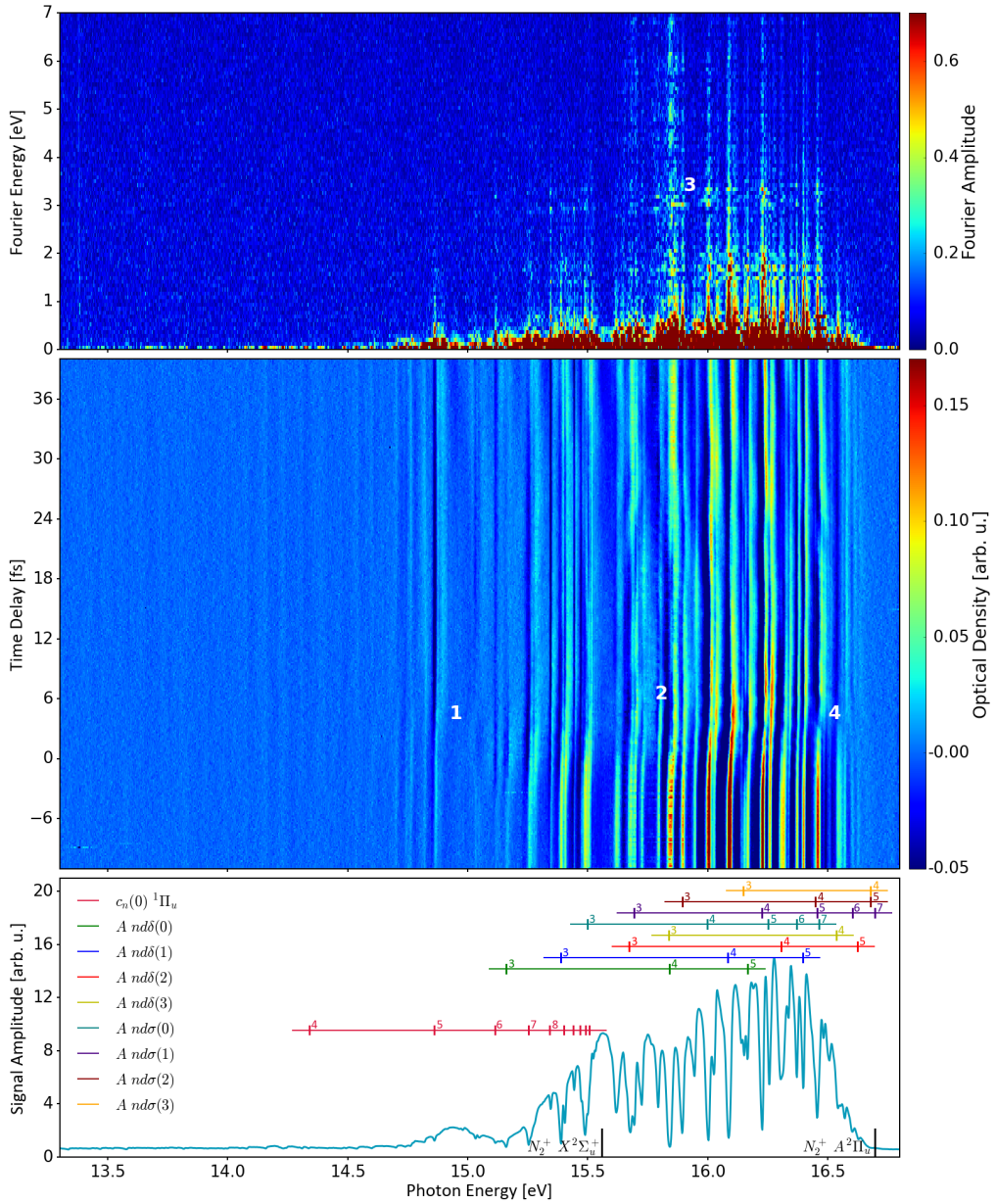

Figure 5.5: The time-delay dependent spectra in nitrogen in the middle and the Fourier spectrum along the time-delay axis on top. Negative time delay means the XUV pulse arrives before the NIR pulse. The NIR peak intensity was ∼3.3 TW/cm^2. Below an absorption spectrum is shown together with the assignment of the states, taken from reference [55] for the c_n states and from [50] for the A states. The two ionization thresholds to the N_2^+ $X^2\Sigma_u^+$ and N_2^+ $A^2\Pi_u$ molecular ion are indicated. For the marked effects seen in the time-delay spectra, see the explanation in the main text.

the measured Fourier spectrum. Because the total time-delay range was limited to ∼51 fs by the walk off of the XUV focus, see chapter 3.2, the resolution is only ∼80 meV in the Fourier energy. Thus, the signal cannot be distinguished from the DC peak. In order to resolve such amplitudes one would need a longer time-delay range, which might be realized by an external translation stage. Here, parts of the NIR pulse could be separately delayed with respect to the XUV pulse and after that both could be coupled into a common beam path. This would cancel the walk-off. However, due to not using the intrinsic time synchronization of the HHG process, it would introduce an extra timing jitter to the two pulses. This setup would therefore limit the time resolution but comes with the benefit of a longer time-delay range, which is the more favorable method for capturing the longer oscillations in the time-delay spectra.

5.2 Intensity scan

The NIR-peak-intensity dependent scan is shown in figure 5.6 for argon and nitrogen. In the scans the optical density is averaged over the time delay of ∼2.5 fs, which corresponds to one full NIR electric-field-cycle. This averages out sub-cycle effects of the dressing electric field. The mean time delay is 5 fs and because the NIR pulse has a pulse duration of ∼7 fs FWHM, the entire pulse comes after the XUV-excitation and can thus maximally affect the target. Various strong-field effects are visible in the scans such as the changes in the absorption line shape with increasing peak intensity, which look like an energy shift for many lines in figure 5.6. This was also observed in helium [27] or different species and it is explained by the phase shift, which the time-dependent dipole moment acquires in the presence of the strong NIR pulse. Some lines in argon start to become independent of the NIR for intensities above ∼6 TW/cm^2 and stay inverted. Many other lines disappear at a certain intensity due to the onset of strong-field ionization of the target gas. Here, the strongly visible $P_{3/2}$ Rydberg series in argon above the first continuum between 15.76 and 15.94 eV show a clear ionization dependency on the principal quantum number. For higher quantum numbers the ionization starts earlier. Below the first ionization threshold in argon also signatures of Autler-Townes splittings [58] are present for a couple of states (figure 5.7).

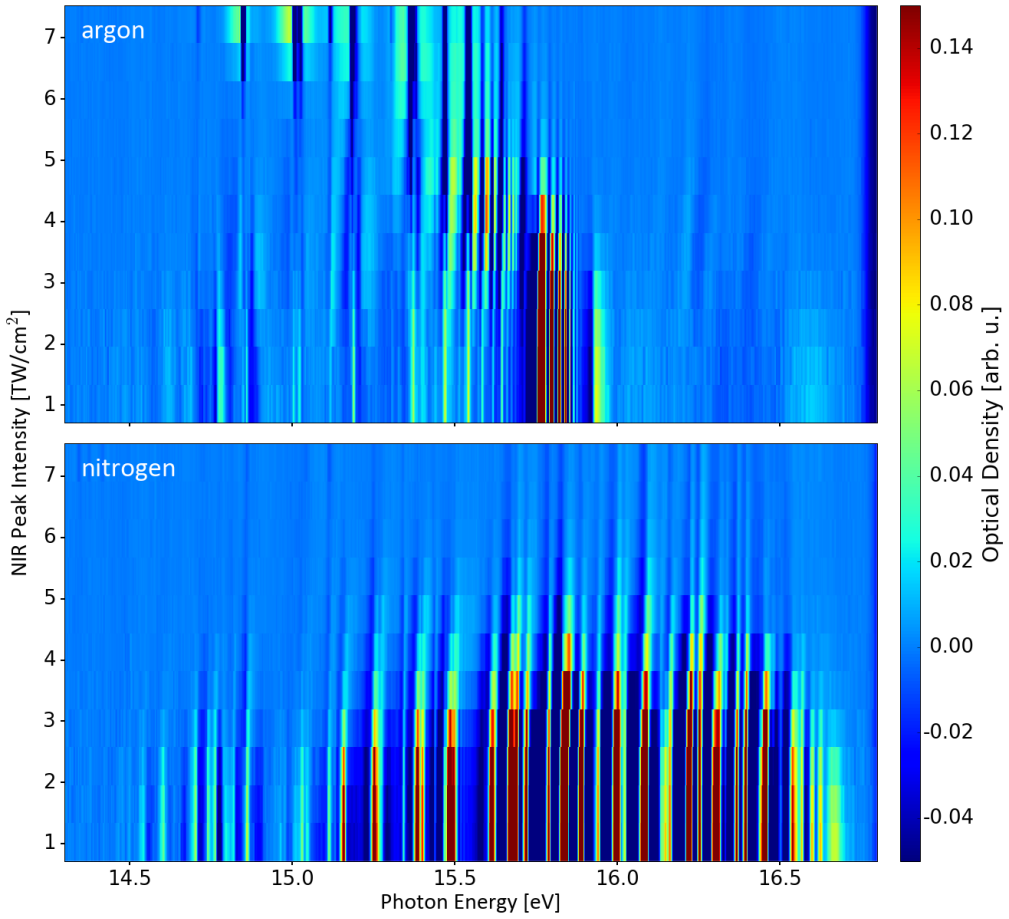

Figure 5.6: NIR peak intensity-dependent absorption spectrum for argon and nitrogen. The optical density is averaged over one full NIR electric-field-cycle of ∼2.5 fs at a central time delay of 5 fs. The data are taken for 11 different iris aperture positions and the peak intensity is calibrated with the procedure explained in chapter 4.5.

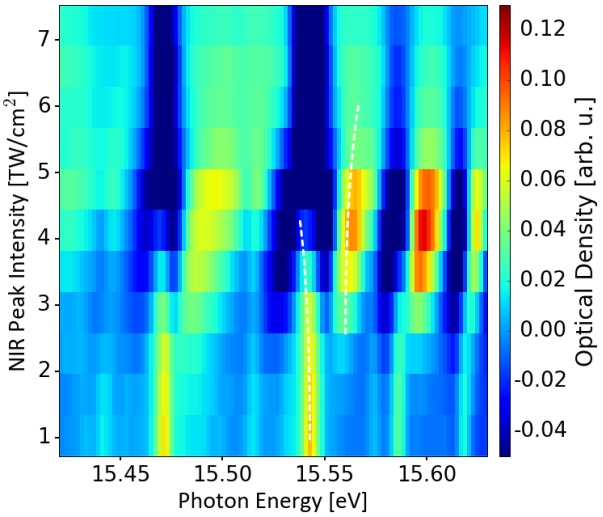

Figure 5.7: Enhanced view of the intensity scan in argon close to the $P_{3/2}$ 10s and $P_{1/2}$ 6d/9s states. Signatures of the Autler-Townes splittings are present which are indicated by white dotted lines.

5.2.1 Laser-imposed phase

In order to quantify the line-shape changes with increasing NIR peak intensity, the lines are fitted by the imaginary part of the energy-dependent dipole moment introduced in the dipole control model, eq 2.40. The fitting procedure in this work follows the Levenberg-Marquardt algorithm [59]. Because some states are closely spaced in energy, they start to overlap when their energy gets shifted. Thus, for some lines it becomes hard to get a reasonable fit throughout the scan. One way out of this problem is to fit multiple lines at the same time by taking a sum of the fit function. However, this leads to less success of the overall fitting routine, in particular if the intensity-dependent line changes are large. Then the initial parameters have to be guessed very precisely. In order to extract the laser-imposed phase, one first has to determine the natural line shape and position by identifying the Fano-phases and energies of the lines without any distortions by the NIR. Therefore, the lines are first fitted at minimum NIR-intensity with fixed zero laser-imposed phase. The value for this Fano-phase might be artificial, caused by the reference spectrum method, which results in optical densities with a missing energy-dependent offset, see chapter 4.6. However, after the Fano-phase is determined, it is fixed together

with the energy position in the following and only changes of the line shape are of interest. Then, the laser-imposed phase is read off of the best fitted curve for every single intensity step.

The figures 5.8 and 5.9 show the extracted laser-imposed phases for two different Rydberg series in argon. The errors are obtained by a residual bootstrapping method, which is explained in the next subsection. The phases behave in a completely different way. Whereas the phases for the $P_{1/2}$ ns/d states increase with higher intensities, the phases of the $P_{3/2}$ ns/d states decrease. However, it is not clear by now whether the opposite behavior is caused by the different spin-orbit configuration of the residual ion core or if this effect is just correlated with e.g. the energy position of the states, because reasonable fits are only obtained for $P_{3/2}$ state, which have lower energies than the $P_{1/2}$ states. The energy position could in principle just determine if the state can couple to different states taking into account the energy bandwidth of the NIR pulse. In order to find the reason for this different behavior, further theoretical studies are needed, which go beyond the scope of this work.

An additional point is that the phase curves are bunched in argon. Nitrogen shows a different behavior for the c_n states (figure 5.10). Their phases are less affected the higher the principle quantum number of the state is. This is also in contrast to previous results in helium [28]. The helium states are more affected the higher the quantum number, which is explained as follows. The excited electron is loosely bound for high-lying states and is thereby less influenced by the residual ion core. If the NIR light hits the system, the nearly-free electron will experience a greater energy shift than in the more tightly bound states. Thus, it gets a larger phase kick by the NIR pulse. The opposite behavior of nitrogen is not understood yet.

5.2.2 Residual bootstrapping

In order to find the errors of the fitting parameters, one can look at the variances given in the fitting procedure. However, the shape of the fitting curve is 2π-periodic in the laser-imposed and Fano-phase making the variances artificially high. An alternative procedure is to use the bootstrapping method, which resamples the recorded data in a determined way and fits it again by the same fit function and initial parameters. This leads to a set of values of fitting

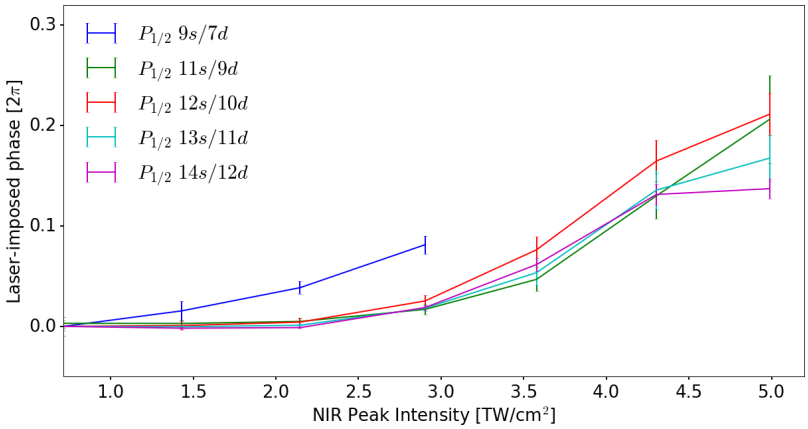

Figure 5.8: Retrieved laser-imposed phases of the $P_{1/2}$ ns/d states in argon versus the NIR peak intensity. For all these states the phase increases with intensity. The bunched curves belong to the states above the first ionization threshold, where the isolated one in blue belongs to the $P_{1/2}$ 9s/7d below the ionization threshold. The latter state seems more affected by the NIR than the others. However, a reasonable fit for this state is only obtained for 4 intensity steps.

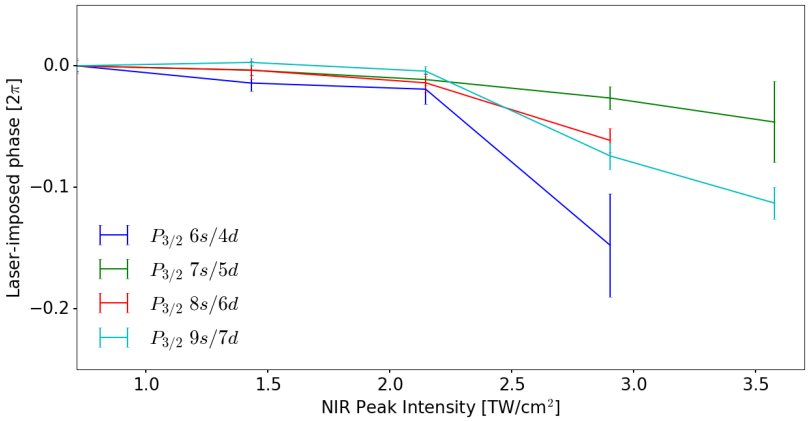

Figure 5.9: Retrieved laser-imposed phase of the $P_{3/2}$ ns/d states in argon versus the NIR peak intensity. For all these states the phase decreases with intensity.

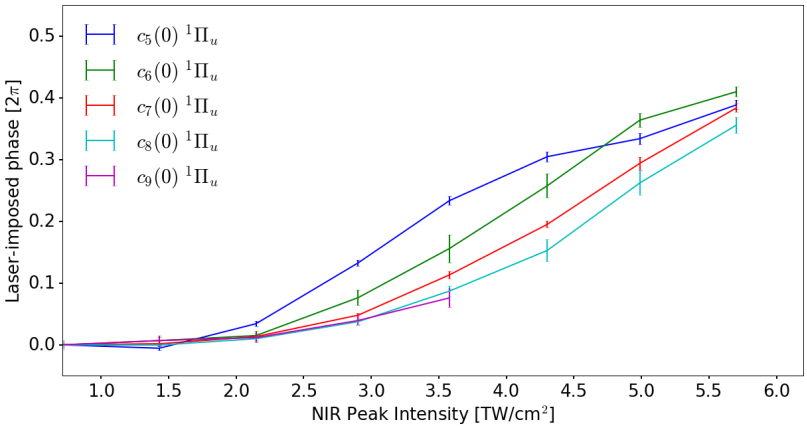

Figure 5.10: Retrieved laser-imposed phase of the $c_n\ ^1\Pi_u$ states with vibronic quantum number $\nu = 0$ in nitrogen versus the NIR peak intensity. The higher the principle quantum number the less the states increase and therewith they are less affected by the NIR pulse.

parameters distributed around the real physical value. The standard deviations of these distributions serve now as the errors in the fitting procedure. Many types of the resampling methods exist for different kinds of problems. Here the residual resampling was used, which first determines the difference between the measured data and the best fitting curve for each data point. This set of differences is called the array of residuals. The next step is to add a residual, which is uniformly drawn from the array of residuals for each data point, to the data value. This is done many times in order to get a big set $(N > 1000)$ of resampled data. Detailed information about bootstrapping methods and their application can be found e.g. in [60].

6 Summary and Outlook

The general topic of this master thesis is the spectroscopic measurement of the transient absorption spectra of argon and molecular nitrogen in the shared energy range of their first ionization threshold between 13 and 17 eV. The measurements were performed with respect to the time delay between an exciting extreme-ultraviolet (XUV) and a manipulating near-infrared (NIR) laser pulse and the NIR intensity. A first evaluation of the measurements was presented. Here, many physical effects, known from previous transient absorption experiments in other species could be observed and interpreted, like line broadening, line-shape modifications and shifts, sub-cycle and slower modulations and strong field ionization. Despite the two-nuclei structure of the molecular nitrogen, its optical density shows a similar time-delay and intensity dependency as the atomic argon. However, in addition couplings of states with low energy differences are visible by means of slow modulations of the optical density with respect to the time delay, e.g. on the order of 20 fs. These modulations could not be resolved in the Fourier spectra due to the limitation of the total time-delay range by the walk-off of the XUV focus in the target. A possible improvement of the experiment could therefore be to use an external translation stage for the control of the time-delay in order to record long time modulations.

For the purpose of the quantification of the line-shape changes, the measured absorption lines were fitted by the imaginary part of the energy-dependent dipole moment, which is proportional to the absorption cross-section. The dependence of this moment on the NIR pulse was theoretically described by a dipole control model. Here, the dipole moment acquires an impulsive phase at the rise of the NIR pulse. This laser-imposed phase is analyzed with respect to the NIR intensity: The retrieved phases of the excited states in argon show a different behavior for different spin-orbit quantum states of the residual ion core. For the total angular momentum quantum number $J = 1/2$ the phases increase and for $J = 3/2$ the phases decrease with the NIR intensity. The phases of the $c_n(0)$ Π_u states of nitrogen show a counterintuitive dependence

on the principle quantum number. The higher the quantum number the less the lines are affected by the NIR pulse. This behavior is the direct opposite compared to the excited states in helium observed in previous experiments [28]. Both effects are not understood so far and therefore further theoretical investigations are needed.

In order to get access to the absorption spectra at energies close to the first ionization threshold of argon and nitrogen at about 15.5 eV, a new grating holder was designed and implemented into the experimental setup. It allows to switch between two gratings for different energy regions under vacuum conditions and with low effort. Furthermore, indium was used as a new filter material, which transmits this low-energy XUV light. However, the transmission is limited to 1.5% and thereby the absorption signal is tremendously attenuated compared to previous experiments, making the whole measurement challenging. The data acquisition time had therefore to be increased and the laser system together with the highly-nonlinear high-harmonic generation process had to be stabilized during that time. Using a thinner filter material would substantially increase the signal. However, these filters are more fragile and a successful measurement could not be realized with them yet. In order to increase the lifetime of the filters, the NIR pulse could be attenuated before it hits the filters. This might be realized by a closed-loop iris or a microchannel plate in front of the filters, which partly blocks or diffracts the NIR pulse and leaves the XUV pulse unaffected [61]. The minimum energy, which could be reached in the experiment, was $\sim$13 eV. However, as the indium filter in principle allow lower energies (figure 3.3) but with less transmission, one could also get access to them if the absorption signal could be increased. At this energies, for example, many valence states in nitrogen lie [55].

The attosecond transient-absorption setup presented here is flexible to many other targets in the spectral range from $\sim$12 to $\sim$70 eV. Future experiments might therefore investigate various diatomic molecules like hydrogen or oxygen as well as more complex molecules like methane. This would be the first organic molecule to be investigated by attosecond transient absorption spectroscopy.

Bibliography

[1] P. M. Paul, E. S. Toma, P. Breger, G. Mullot, F. Auge, P. Balcou, H. G. Muller, and P. Agostini. *Observation of a train of attosecond pulses from high harmonic generation.* Science **292**, 1689–1692 (2001).

[2] A. H. Zewail. *Femtochemistry.* J. Phys. Chem. **97**, 12427–12446 (1993).

[3] E. Goulielmakis, Z.-H. Loh, A. Wirth, R. Santra, N. Rohringer, V. S. Yakovlev, S. Zherebtsov, T. Pfeifer, A. M. Azzeer, M. F. Kling, S. R. Leone, and F. Krausz. *Real-time observation of valence electron motion.* Nature **466**, 739–743 (2010).

[4] C. Ott, A. Kaldun, L. Argenti, P. Raith, K. Meyer, M. Laux, Y. Zhang, A. Blättermann, S. Hagstotz, T. Ding, et al. *Reconstruction and control of a time-dependent two-electron wave packet.* Nature **516**, 374–378 (2014).

[5] M. Chini, B. Zhao, H. Wang, Y. Cheng, S. X. Hu, and Z. Chang. *Subcycle ac Stark Shift of Helium Excited States Probed with Isolated Attosecond Pulses.* Phys. Rev. Lett. **109**, 073601 (2012).

[6] S. Chen, M. J. Bell, A. R. Beck, H. Mashiko, M. Wu, A. N. Pfeiffer, M. B. Gaarde, D. M. Neumark, S. R. Leone, and K. J. Schafer. *Light-induced states in attosecond transient absorption spectra of laser-dressed helium.* Phys. Rev. A **86**, 063408 (2012).

[7] H. Mashiko, K. Oguri, T. Yamaguchi, A. Suda, and H. Gotoh. *Petahertz optical drive with wide-bandgap semiconductor.* Nat. Phys. pp. 1745–2481 (2016).

[8] S. R. Leone, C. W. McCurdy, J. Burgdörfer, L. S. Cederbaum, Z. Chang, N. Dudovich, J. Feist, C. H. Greene, M. Ivanov, R. Kienberger, et al. *What will it take to observe processes in 'real time'?* Nat. Phot. **8**, 162–166 (2014).

[9] F. Lépine, M. Y. Ivanov, and M. J. Vrakking. *Attosecond molecular dynamics: fact or fiction?* Nat. Phot. **8**, 195–204 (2014).

[10] M. Kowalewski, K. Bennett, K. E. Dorfman, and S. Mukamel. *Catching Conical Intersections in the Act: Monitoring Transient Electronic Coherences by Attosecond Stimulated X-Ray Raman Signals.* Phys. Rev. Lett. **115**, 193003 (2015).

[11] G. Sansone, M. Reduzzi, A. Dubrouil, C. Feng, M. Nisoli, F. Calegari, C. D. Lin, W. C. Chu, L. Poletto, and F. Frassetto. *Attosecond Absorption Spectroscopy in molecules.* In *CLEO: 2013*. Optical Society of America (2013).

[12] Y. Cheng, M. Chini, X. Wang, Y. Wu, and Z. Chang. *Attosecond Transient Absorption in Molecular Hydrogen.* In *CLEO: 2014*. Optical Society of America (2014).

[13] J. E. Bækhøj, L. Yue, and L. B. Madsen. *Nuclear-motion effects in attosecond transient-absorption spectroscopy of molecules.* Phys. Rev. A **91**, 043408 (2015).

[14] E. R. Warrick, W. Cao, D. M. Neumark, and S. R. Leone. *Probing the Dynamics of Rydberg and Valence States of Molecular Nitrogen with Attosecond Transient Absorption Spectroscopy.* J. Phys. Chem. A (2016).

[15] M. Reduzzi, W.-C. Chu, C. Feng, A. Dubrouil, J. Hummert, F. Calegari, F. Frassetto, L. Poletto, O. Kornilov, M. Nisoli, C.-D. Lin, and G. Sansone. *Observation of autoionization dynamics and sub-cycle quantum beating in electronic molecular wave packets.* J. Phys. B **49**, 065102 (2016).

[16] J.-C. Diels and W. Rudolph. *Ultrashort Laser Pulse Phenomena.* Second Edition. Academic Press (2006).

[17] Z. Chang. *Fundamentals of Attosecond Optics.* CRC Press Taylor & Francis Group (2011).

[18] B. E. A. Saleh and M. C. Teich. *Fundamentals of Photonics.* Second Edition. Wiley (2007).

[19] T. Brabec and F. Krausz. *Intense few-cycle laser fields: Frontiers of nonlinear optics.* Rev. Mod. Phys. **72**, 545–591 (2000).

[20] P. Agostini and L. F. DiMauro. *The physics of attosecond light pulses.* Rep. Prog. Phys. **67**, 813 (2004).

[21] F. Krausz and M. Ivanov. *Attosecond physics.* Rev. Mod. Phys. **81**, 163–234 (2009).

[22] K. Zhao, Q. Zhang, M. Chini, Y. Wu, X. Wang, and Z. Chang. *Tailoring a 67 attosecond pulse through advantageous phase-mismatch.* Opt. Lett. **37**, 3891–3893 (2012).

[23] P. B. Corkum. *Plasma perspective on strong field multiphoton ionization.* Phys. Rev. Lett. **71**, 1994–1997 (1993).

[24] A. D. Shiner, C. Trallero-Herrero, N. Kajumba, H.-C. Bandulet, D. Comtois, F. Légaré, M. Giguère, J.-C. Kieffer, P. B. Corkum, and D. M. Villeneuve. *Wavelength Scaling of High Harmonic Generation Efficiency.* Phys. Rev. Lett. **103**, 073902 (2009).

[25] P. B. Corkum and F. Krausz. *Attosecond science.* Nature Phys. **3**, 381–387 (2007).

[26] U. Fano. *Effects of Configuration Interaction on Intensities and Phase Shifts.* Phys. Rev. **124**, 1866–1878 (1961).

[27] C. Ott, A. Kaldun, P. Raith, K. Meyer, M. Laux, J. Evers, C. H. Keitel, C. H. Greene, and T. Pfeifer. *Lorentz Meets Fano in Spectral Line Shapes: A Universal Phase and Its Laser Control.* Science **340**, 716–720 (2013).

[28] A. Blättermann, C. Ott, A. Kaldun, T. Ding, V. Stooß, M. Laux, M. Rebholz, and T. Pfeifer. *In situ characterization of few-cycle laser pulses in transient absorption spectroscopy.* Opt. Lett. **40**, 3464–3467 (2015).

[29] A. Blättermann, C. Ott, A. Kaldun, T. Ding, and T. Pfeifer. *Two-dimensional spectral interpretation of time-dependent absorption near laser-coupled resonances.* J. Phys. B **47**, 124008 (2014).

[30] A. Blättermann. *Impulsive control of the atomic dipole response in the time and frequency domain.* PhD Thesis, University of Heidelberg (2016).

[31] C. Ott. *Attosecond multidimensional interferometry of single and two correlated electrons in atoms.* PhD Thesis, University of Heidelberg (2012).

[32] M. Schönwald. *Phase-matched few-cycle high-harmonic generation: ionisation gating and half-cycle cutoffs.* Diploma Thesis, University of Heidelberg (2010).

[33] V. Stooss. *Time-resolved strong field effects in Helium observed with transient absorption spectroscopy.* Master's thesis, University of Heidelberg (2015).

[34] A. M. Zheltikov. *Ultrashort light pulses in hollow waveguides.* Physics-Uspekhi **45**, 687 (2002).

[35] M. D. Hartmann. *Characterization of Few-Cycle Laser Pulses.* Master's thesis, University of Heidelberg (2016).

[36] http://henke.lbl.gov/optical_constants/.

[37] A. Kaldun. *Fano Resonances in the Time Domain - understanding and controlling the absorption and emission of light.* PhD Thesis, University of Heidelberg (2014).

[38] T. Ding, C. Ott, A. Kaldun, A. Blättermann, K. Meyer, V. Stooss, M. Rebholz, P. Birk, M. Hartmann, A. Brown, H. V. D. Hart, and T. Pfeifer. *Time-resolved four-wave-mixing spectroscopy for inner-valence transitions.* Opt. Lett. **41**, 709–712 (2016).

[39] W. Demtröder. *Experimentalphysik 1.* Springer Spektrum (2015).

[40] https://www.webelements.com/.

[41] H. A. Rowland. *XXIX. On concave gratings for optical purposes.* Philos. Mag. Ser. 5 **16**, 197–210 (1883).

[42] https://hitachi-hta.com/sites/default/files/ConcaveGrating Spectrograph-Grazing%281%29_0.pdf.

[43] S. L. Sorensen, T. Åberg, J. Tulkki, E. Rachlew-Källne, G. Sundström, and M. Kirm. *Argon 3 s autoionization resonances.* Phys. Rev. A **50**, 1218–1230 (1994).

[44] http://www.nist.gov/pml/data/asd.cfm.

[45] J. Nentwig. *Kunststoff-Folien: Herstellung, Eigenschaften, Anwendung.* Third edition. Carl Hanser Verlag (2006).

[46] J. Itatani, F. Quéré, G. L. Yudin, M. Y. Ivanov, F. Krausz, and P. B. Corkum. *Attosecond Streak Camera.* Phys. Rev. Lett. **88**, 173903 (2002).

[47] T. Ding. *Time-resolved spectroscopy of autoionizing states in few-electron systems.* Master Thesis, University of Heidelberg (2013).

[48] W. M. Kosman and S. Wallace. *Complete dipole oscillator strength distribution and its moments for N2.* J. Chem. Phys. **82**, 1385–1399 (1985).

[49] K. Huber and C. Jungen. *High-resolution jet absorption study of nitrogen near 800 Å.* J. Chem. Phys. **92**, 850–861 (1990).

[50] H. Lefebvre-Brion and K. Yoshino. *Tentative Interpretation of the Rydberg Series Converging to the $A^2\ \Pi_u$ State of $N^+{}_2$.* J. Mol. Spec. **158**, 140–146 (1993).

[51] M. Sommavilla, U. Hollenstein, G. M. Greetham, and F. Merkt. *High-resolution laser absorption spectroscopy in the extreme ultraviolet.* J. Phys. B **35**, 3901 (2002).

[52] H. Lefebvre-Brion. *Assignment in the near-threshold absorption spectrum of N_2.* J. Chem. Phys. **122** (2005).

[53] M. Sommavilla and F. Merkt. *On the rotational structure of a prominent band in the vacuum-ultraviolet spectrum of molecular nitrogen.* J. Elect. Spec. and Rel. Phen. **151**, 31 – 33 (2006).

[54] J. B. Randazzo, P. Croteau, O. Kostko, M. Ahmed, and K. A. Boering. *Isotope effects and spectroscopic assignments in the non-dissociative photoionization spectrum of N_2.* J. Chem. Phys. **140** (2014).

[55] A. Lofthus and P. H. Krupenie. *The spectrum of molecular nitrogen.* J. Phys. Chem. Ref. Data **6**, 113–307 (1977).

[56] X. Wang, M. Chini, Y. Cheng, Y. Wu, X.-M. Tong, and Z. Chang. *Subcycle laser control and quantum interferences in attosecond photoabsorption of neon.* Phys. Rev. A **87**, 063413 (2013).

[57] W. Cao, E. R. Warrick, D. M. Neumark, and S. R. Leone. *Attosecond transient absorption of argon atoms in the vacuum ultraviolet region: line energy shifts versus coherent population transfer.* New J. Phys. **18**, 013041 (2016).

[58] S. H. Autler and C. H. Townes. *Stark Effect in Rapidly Varying Fields.* Phys. Rev. **100**, 703–722 (1955).

[59] D. W. Marquardt. *An algorithm for least-squares estimation of nonlinear parameters.* J. Soc. Ind. App. Math. **11**, 431–441 (1963).

[60] B. Efron. *Bootstrap Methods: Another Look at the Jackknife.* Ann. Statist. **7**, 1–26 (1979).

[61] Q. Zhang, K. Zhao, J. Li, M. Chini, Y. Cheng, Y. Wu, E. Cunningham, and Z. Chang. *Suppression of driving laser in high harmonic generation with a microchannel plate.* Opt. Lett. **39**, 3670–3673 (2014).

Danksagung

Ich möchte allen aus der Interatto/X-MuSIC Gruppe für die nette, lehrreiche und immer wieder unterhaltsame Stunden während dieser Masterarbeit danken. Einen besonderen Dank geht an…

Prof. Dr. Thomas Pfeifer, der mir die Möglichkeit für diese Arbeit gegeben hatte, indem er mich in seine Forschungsgruppe aufnahm. Ich finde es faszinierend, dass er zu jedem Thema in der Physik immer irgendwie mitreden kann und dass er trotz hohem Arbeitspensum doch irgendwie immer erreichbar ist,
Priv.-Doz. Dr. Robert Moshammer, der sich freundlicherweise dazu bereit erklärt hatte, diese Masterarbeit als Zweitgutachter zu betreuen,
Veit Stooß für die etlichen Stunden im Labor und für sein Engagement auch nachts bis um 5 oder 6 Uhr morgens mit mir Messungen zu machen,
Maximilian Hartmann, für die viele Zeit bei der gemeinsamen Justage von Optiken. Diese Zeit hatte ich genießen können. Er war es auch, der die wesentlichen Teile meiner Arbeit gelesen und für mich berichtigen konnte,
Dr. Alexander Blättermann für seinen atembraubenden Charme am Kickertisch und dass ich an seinen Erfahrungen am Laser und am Experiment, teilhaben durfte,
Martin Laux für die vielen lustigen Unterhaltungen die wir miteinander führen konnten,
Dr. Kristina Meyer und **Dr. Andreas Kaldun** die immer ein offenes Ohr für mich hatten,
die X-MuSICians: Thomas Ding, Marc Rebholz und Lennart Aufleger für eure entspannte Atmosphäre.

Einen speziellen Dank geht an meine **Judith**, die allein Zuhause mit unserer Tochter auf mich wartet, während ich diese Zeilen hier schreibe. Danke für dein Verständnis, wenn ich mal länger bei der Arbeit bin, danke für den Rückhalt, den du mir besonders bei unserem gemeinsamen Kind während dieser Arbeit gegeben hattest. Danke, dass du immer für mich da bist.

Erklärung:

Ich versichere, dass ich diese Arbeit selbstständig verfasst, und keine anderen als die angegebenen Quellen und Hilfsmittel benutzt habe.

Heidelberg, den 29. April 2016 . . . . . .